Space Sci Rev (2007) 132: 399–431
DOI 10.1007/s11214-007-9221-3

Mercury's Surface Composition and Character as Measured by Ground-Based Observations

A. Sprague · J. Warell · G. Cremonese · Y. Langevin · J. Helbert · P. Wurz · I. Veselovsky · S. Orsini · A. Milillo

Received: 29 January 2007 / Accepted: 24 May 2007 / Published online: 10 October 2007

Abstract Mercury's surface is thought to be covered with highly space-weathered silicate material. The regolith is composed of material accumulated during the time of planetary formation, and subsequently from comets, meteorites, and the Sun. Ground-based observations indicate a heterogeneous surface composition with SiO_2 content ranging from 39 to 57 wt%. Visible and near-infrared spectra, multi-spectral imaging, and modeling indicate expanses

A. Sprague (✉)
Lunar and Planetary Laboratory, University of Arizona, Tucson, AZ 85721, USA
e-mail: sprague@lpl.arizona.edu

J. Warell
Department of Astronomy and Space Physics, Uppsala University, 75120 Uppsala, Sweden

G. Cremonese
INAF-Osservatorio Astronomico, vic.Osservatorio 5, 35122 Padova, Italy

Y. Langevin
Institut d'Astrophysique Spatiale, CNRS/Univ. Paris XI, 91405 Orsay, France

J. Helbert
Institute for Planetary Research, DLR, Rutherfordstrasse 2, 12489 Berlin, Germany

P. Wurz
Physics Institute, University of Bern, Sidlerstrasse 5, 3012 Bern, Switzerland

I. Veselovsky
Skobeltsyn Institute of Nuclear Physics, Moscow State University, 119992 Moscow, Russia

I. Veselovsky
Space Research Institute (IKI), Russian Academy of Sciences, 117997, Moscow, Russia

S. Orsini · A. Milillo
Istituto di Fisica dello Spazio Interplanetario (IFSI), via del Fosso del Cavaliere, 100,00133, Rome, Italy

S. Orsini · A. Milillo
Istituto Nazionale di Astrofisica (INAF), via del Fosso del Cavaliere, 100,00133, Rome, Italy

of feldspathic, well-comminuted surface with some smooth regions that are likely to be magmatic in origin with many widely distributed crystalline impact ejecta rays and blocky deposits. Pyroxene spectral signatures have been recorded at four locations. Although highly space weathered, there is little evidence for the conversion of FeO to nanophase metallic iron particles ($npFe^0$), or "iron blebs," as at the Moon. Near- and mid-infrared spectroscopy indicate clino- and ortho-pyroxene are present at different locations. There is some evidence for no- or low-iron alkali basalts and feldspathoids. All evidence, including microwave studies, point to a low iron and low titanium surface. There may be a link between the surface and the exosphere that may be diagnostic of the true crustal composition of Mercury. A structural global dichotomy exists with a huge basin on the side not imaged by Mariner 10. This paper briefly describes the implications for this dichotomy on the magnetic field and the 3 : 2 spin : orbit coupling. All other points made above are detailed here with an account of the observations, the analysis of the observations, and theoretical modeling, where appropriate, that supports the stated conclusions.

Keywords Mercury · Planetary surface composition · Mercury's surface composition · Remote sensing · Ground-based observations · Spectroscopy

1 Introduction

Mariner 10 made no direct measurements of Mercury's surface composition (for details see "The Surface of Mercury as seen by Mariner 10," by Cremonese et al. 2007, this issue). The vidicon cameras imaged 45% of Mercury's surface and showed it to be heavily cratered; in that sense, it resembles the Moon. Also, the crater morphology and tectonic expression of fault scarps and ejecta rays give the strong impression that the surface is covered with silicates. Ground-based imaging of the remaining 55% of Mercury's surface, in the visible and near-IR, microwave, and radar wavelengths, have found a surface similar to that found by Mariner 10—highly cratered, along with a huge basin and several locations of unusually bright visible and radar spots (for details see "Earth-based Visible and Near-IR Imaging of Mercury," by Ksanfomality et al. 2007, this issue). Ground-based telescopic spectroscopy has identified key spectral signatures that support the Mariner 10 impression of a heavily cratered, silicate surface. Several spectra have been interpreted in terms of Mercury's surface composition. The effects of space weathering and exogenic material on the spectral signatures are probably significant and must be accounted for in our spectral analysis, modeling, and interpretations.

Much work has occurred in the past decade, and this article focuses on these new results but also gives a review of older research, permitting the interested reader to find historical material. Also included are brief descriptions of laboratory spectral measurements of terrestrial, lunar, and meteoritic rocks, and minerals (at a variety of grain sizes) where necessary for complete description of the Mercury science. Laboratory spectral libraries are critical for the interpretation of spectra, especially from Mercury, a body for which we have no known "ground truth." All of the ground-based discoveries are discussed in the context of the challenges and opportunities of future ground-based observations and orbital measurements by the MESSENGER and Bepi Colombo spacecrafts.

2 Visible and Near Infrared Measurements of Mercury's Surface

Observational studies of visible and near infrared spectra of Mercury (wavelength range 0.4–2.5 μm) have been performed since the 1960s with a variety of techniques. Concise

reviews of these efforts are given in, e.g., Vilas et al. (1988, 1984), Blewett et al. (1997) and Warell (2003). The techniques include filter photometry (Harris 1961; Irvine et al. 1968; Warell 2002), CVF photoelectric photometry (McCord and Adams 1972a, 1972b; Vilas and McCord 1976; Tepper and Hapke 1977; McCord and Clark 1979; Vilas et al. 1984), and low-resolution reflectance spectroscopy (Vilas 1985; Warell 2003; Warell and Blewett 2004; Warell et al. 2006). Papers since 2002 include disk-resolved data sets, while the earlier observations were made of the integrated disk.

Descriptions of the physics of absorption bands in the VISNIR have been reviewed by many authors (e.g., Burns 1993; Gaffey et al. 1993; Hapke 2001; Pieters and Englert 1993) and will not be repeated here. The two most sought-after bands in this wavelength region are the 1 μm crystal field band due to ferrous iron in crystalline silicates, and the very strong oxygen–metal charge transfer bands of iron and titanium oxides in the near-UV, below 0.5 μm. Historically, there has been much debate about the presence of the ferrous iron band in spectra obtained in the 1960s to 1990s, though it now appears to have been detected (Warell et al. 2006). The near-UV absorption edge has not been identified with certainty. This failure may be related to the strong maturity (highly space weathered) of the surface and to minute abundances of titanium in the crustal rocks.

The spectroscopic observations of Mercury obtained before the mid-1990s were rigorously analyzed by Blewett et al. (1997) in order to constrain Mercury's surface composition. The best spectra indicated an FeO content of 3% and a TiO_2 content of 1%, based on the color-ratio analysis methods formulated and calibrated for the Moon by Lucey et al. (1998, 2000).

Hapke (2001), using his improved model for light scattering in particulate semi-transparent media, summarized the present knowledge of Mercury based on Mariner 10 and ground-based spectroscopic studies to indicate the presence of a crust low in, but not devoid of, ferrous iron with an abundance of submicroscopic metallic iron that is similar to the Moon's, about 0.5 wt%.

Blewett et al. (2002) compared the spectra of a number of small, highly mature and iron-poor sites of the lunar farside (obtained during the Clementine Mission) with those of Mercury. A distinct difference between the lunar pure anorthosite (>90% plagioclase feldspar) regions compared to mercurian spectra is that the lunar spectra have a marked ferrous iron absorption band at 1 μm, clearly visible despite the very low abundance of FeO (2.8–3.3 wt%) and the fact that the Clementine photometry does not cover the full wavelength range of the band. Also, the lunar spectra were found to be slightly less sloped at wavelengths shorter than 0.75 μm than their mercurian counterparts. An explanation put forth by Blewett et al. (2002) is that Mercury's regolith has very little $npFe^0$.

The multicolor photometric imaging observations reported by Warell (2002) effectively covered the integral disk between 47°–236°E longitudes, on primarily the poorly known hemisphere. These data support the inferences from the first mercurian CCD spectrum obtained by Vilas (1985), covering 105°–227°E, indicating a strongly sloped and linearly shaped spectrum from 550–940 nm with no indication of the presence of a 1 μm ferrous absorption band. The disk-resolved nature of the imaging observations allowed the study of spectra of individual bright and dark albedo features, but the spectra of these two groups of features were not statistically different except for reflectance value. One finding was the presence of an inverse relation of the spectral slope with the emission angle, such that features at mid-disk have the steepest slopes. This effect was much stronger than the case for returned samples of the lunar regolith, for which it was proposed to be a result of wavelength-dependent backscattering efficiency—stronger than the case for (disturbed) lunar material. The spectral slope-photometric geometry relation was suggested as due to the presence of a

greater abundance of complex, backscattering agglutinates (glassy regolith particles somewhat larger than average formed in the space weathering process) with absorption efficiencies smaller than those of their lunar counterparts.

Warell (2003) acquired 520–970 nm spectra from 60°–120°E longitudes in 1999 that support most of the previous work in terms of absence of the 1 μm absorption band and that verify the marked spectral slope-photometric geometry relation of Warell (2002). Spectral modeling with the light-scattering theory of Hapke (2001), which had previously not been rigorously applied to mercurian spectra, implied that the metallic iron abundance is likely less than 0.3%, and that modeled ferrous content (<3 wt%) in mercurian materials is lower than in lunar materials.

Noble and Pieters (2001) made a theoretical prediction of a spectral effect due to Ostwald ripening which might be operating on Mercury. This process involves an increase in the size of $npFe^0$ particles at elevated temperatures, and was postulated to be important at surface temperatures above about 470 K (Mercury's equatorial temperature exceeds this value by up to 250 K at local noon). The spectral result of coarsening metallic iron particles at equatorial and low mid-latitudes would be a general decrease in reflectance in the VIS–NIR range, in contrast to a strong reddening for the case of smaller (4–33 nm) particles which cause both darkening and reddening. The spectral manifestation of this prediction was checked by Warell (2003) using the disk-resolved data set of Warell (2002), and indications of the expected increase of spectral slope (reddening) with higher latitude was found.

A set of new CCD spectra of Mercury covering the blue range (0.40–0.65 μm) were combined by Warell and Blewett (2004) with previously obtained spectra and rigorously modeled with the improved Hapke (2002) theory to derive quantitative compositional information. The 0.6–2.5 μm CVF photometer disk-integral spectrum of McCord and Clark (1979), at the time the only published NIR spectrum of Mercury, and a synthetic 0.40–0.97 μm Mercury spectrum derived for standard observational geometry, were used to constrain the range of compositional models. Hapke-model physical parameters used in the analysis were based on modeling of well-characterized laboratory spectra of synthetically matured silicates, laboratory lunar regolith samples, and remotely sensed lunar pure anorthosite regions. Contrary to the case for the strongly spectrally sloped lunar pure anorthosite regions, the slope of the redder mercurian spectrum could not be explained without the assumption of a wavelength dependence in the amplitude of the backscattering lobe of the double Henyey-Greenstein single particle scattering function. For Mercury, the best-fit models consisted of a high reflectance labradorite plagioclase mixed with a minor amount of low-iron enstatite pyroxene, yielding an FeO abundance of 1.2 wt%. The abundance of submicroscopic metallic iron cannot be determined without knowledge of the average optically active grain size, which is unknown. However, grain sizes of the order of 30 μm or less (half the size of lunar particulate materials), were found to be the best fit of for all the modeled spectra. With that result, the wt% $npFe^0$ must be about 0.1 wt%, and likely to be from exogenic sources.

After an observational quest lasting about 40 years, it appears that an absorption band in the near-infrared spectrum of Mercury finally has been identified (Fig. 1). Warell et al. (2006) presented disk-resolved spectra for the 0.7–5.3 μm range with the SpeX instrument at the NASA Infrared Telescope Facility (IRTF) on Mauna Kea, HI. Two near-polar spectra showed the presence of broad shallow bands centered at about 1.1 μm. Their shapes and widths are consistent with the presence of Ca-rich clinopyroxene in various amounts in a highly matured regolith which is heterogeneous in composition on regional scales of 200 km or so. These results support the results of mid-infrared (3–14 μm) spectral studies of Sprague et al. (2002) who obtained Mercury emissivity spectra exhibiting spectral features similar to those of laboratory Ca-rich diopside.

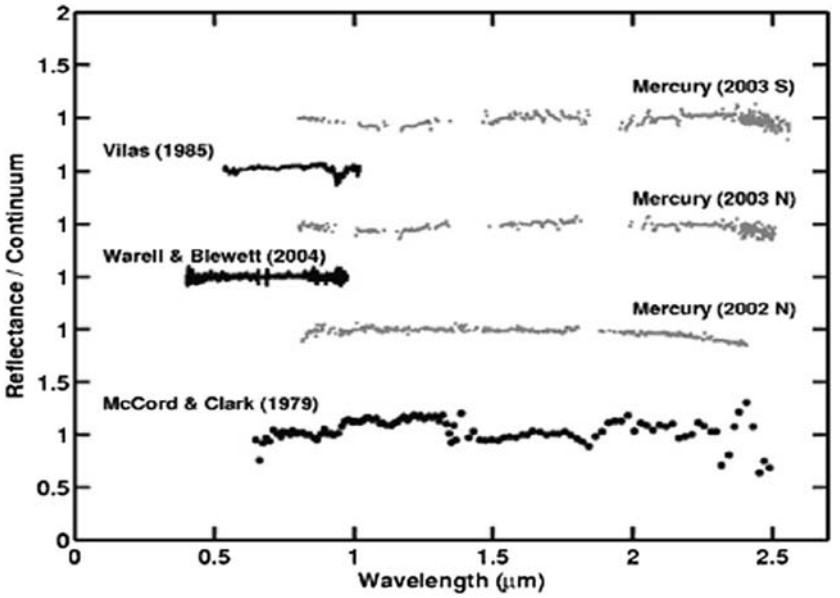

Fig. 1 First spectra to unambiguously show reflectance absorption near 1 μm (2003S, 2003N, 2002N) compared to previous efforts (Vilas, Warell, and Blewett; McCord and Clark). The strong red slope of the continuum has been divided out of these spectra to enhance the visibility of the absorption bands in the 2003S and 2003N spectra. From Warell et al. (2006)

2.1 General Summary and Implications of Vis- and Near-IR Spectroscopic Observations

The effective footprints of the mercurian spectroscopic targets are often large in ground-based observations (up to many hundreds of km) because of smearing by Earth's atmospheric turbulence. Thus, the sampled surface regions include a range of geologic units, many of which are probably highly space weathered. The spectroscopic signature of particularly interesting formations, possessing more crystalline crustal materials than the average surface, are present in the spectral footprints to smaller or larger extents depending on location. Such features are typically too small in areal extent to provide enough flux to dominate the observed spectra. Ideally, remote-sensing studies should be targeted to small and well-defined surface locations which are immature and contain a significant crystalline component. In addition, the exposed rocks should be excavated from depth to sample the native crust, and not merely represent the reprocessed local surface regolith such as breccias with a substantial exogenic component. With slit spectroscopy and the newer, sensitive instruments like SpeX, for 0.8- to 5-μm measurements, and the **M**id**I**nfra**R**ed**S**pectrometer&**I**mager (MIRSI), both at the IRTF, such smaller (200- to 300-km expanses) areal observations are possible. In this respect, it is interesting to note that the identification of absorption bands due to crystalline high-Ca pyroxene in two SpeX spectra from polar regions of Mercury (Warell et al. 2006) were made in surface regions where albedo maps indicate the presence of optically bright terrain, likely to have some exposed fresh material. Another site at which no band was detected was located in an optically dark surface region, likely to be highly space weathered.

Spectra from previously deep-seated crustal material make studies of the bulk material composition possible. Interior walls with mass-wasting morphologies, uplifted central

peaks, and blocky ejecta blankets of young craters will be obvious targets for specific studies with MESSENGER and BepiColombo instrumentation. Also interesting will be other types of surface units likely to expose large amounts of crystalline material, such as lobate scarp faults.

3 Mid-Infrared Spectroscopy of Mercury's Surface

3.1 Laboratory Studies of Mid-Infrared Spectral Emission from Rocks and Minerals

Detailed mid-infrared laboratory studies of rock and mineral samples were begun by Logan and Hunt (1970), Salisbury et al. (1994), Henderson and Jakosky (1997), Wagner (2000), and others. More sophisticated laboratory study is now underway as part of the preparation for the Bepi Colombo mission to Mercury (Benkhoff et al. 2006; Maturilli et al. 2006a, 2006b) in the Planetary Emissivity Laboratory (PEL) at DLR. Currently these measurements are performed under ambient conditions, using a device built at DLR (Berlin) and coupled to a Fourier transform infrared spectrometer Bruker IFS 88 purged with dry air and equipped with a liquid-nitrogen-cooled MCT detector. In the near future measurements under vacuum conditions and in temperature ranges more applicable to Mercury are planned using a Bruker VERTEX 80v spectrometer and new detectors which allow measurement of the emissivity of samples in the wavelength range from 1 to 50 μm.

Figure 2 shows emissivity spectra obtained as part of the Berlin Emissivity Database (BED) under ambient conditions (Maturilli et al. 2006b). In general, spectra of the different mineral classes and subclasses can be easily distinguished from the high variability in positions and shapes of the major emissivity features. Three main spectral regions are: Christiansen feature (also the Emissivity Maximum-EM), the Reststrahlen bands (RB), and the Transparency Minima (TM). Hapke (1996) demonstrated that the actual wavelength of the Christiansen feature does not always coincide exactly with the EM which is the true diagnostic emissivity feature in silicates. In the spectra of silicates, The EM and TM shift to lower wave numbers (longer wavelengths) with decreasing polymerization degree of SiO_4 tetrahedra (Conel 1969). Therefore, these features are located at longer wavelengths in the emission spectra of olivines, compared to those of feldspars.

There is also a strong influence of particle size on the characteristics and shape of emittance spectra. This is well known but has often been neglected when studying the composition of planetary surfaces in the mid-infrared wavelength range. One reason for this neglect was the lack of a database with true emission spectra for a grain sizes less than 125 μm. The BED spectral library now contains entries for planetary analogue materials, separated in well-defined grain size ranges: $<$25 μm, 25–63 μm, 63–125 μm, and 125–250 μm. These grain sizes are ideal for application to thermal emittance spectra from Mercury because Mercury's regolith is highly comminuted and likely covered with fine dust of native and exogenic material.

The positions and shapes of RBs are specific for the chemistry and lattice structures of the particular material. The band depths and shapes are strongly affected by particle size and crystal orientation. In general an increase in the spectral contrast can be observed going from fine to coarse grain sizes. For size separates smaller than 25 μm, the contribution of volume scattering is significant. For these small particles, the spectral contrast within the Reststrahlen bands is strongly reduced and a separate emission minimum is mostly evident at about 800 to 870 cm^{-1} (11.5–12.5 μm). This emissivity minimum (TM), is a highly diagnostic spectral feature which is present as a maximum in reflectance spectra of fine-grained minerals and rocks. However, its wavelength position in the spectra of silicates

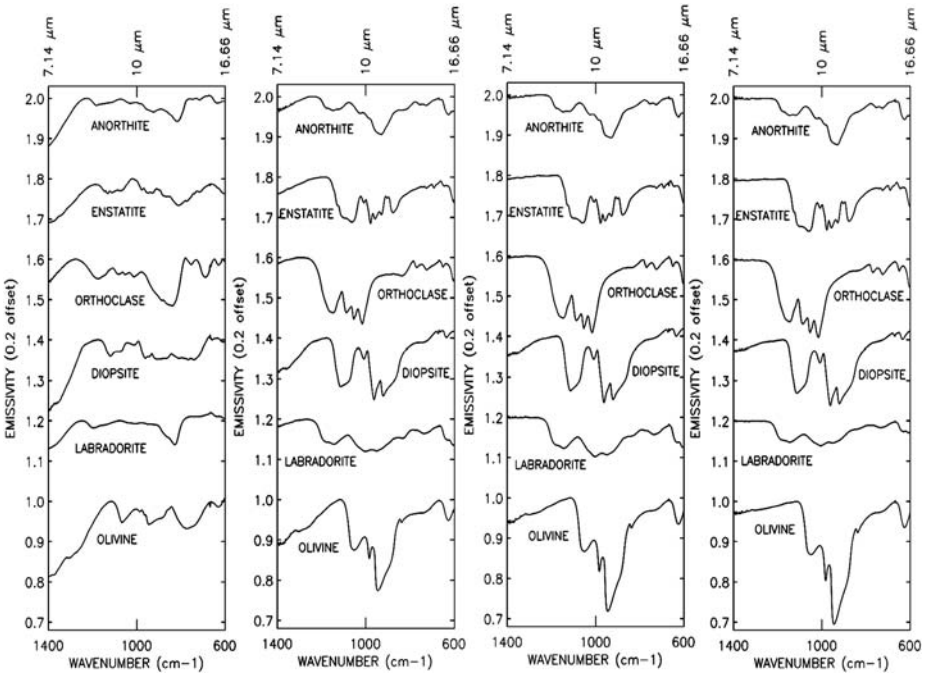

Fig. 2 True emissivity spectra of some of the MERTIS analogue materials (Benkhoff et al. 2006) obtained as part of the BED (Maturilli et al. 2006a, 2006b). Grain size fractions from left to right: <25 μm, 25–63 μm, 63–125 μm, and 125–250 μm. All spectra show some contribution from residual water vapor in the chamber at wave numbers higher than 1,300 cm^{-1}

is affected by particle size (Mustard and Hays 1997). The Christiansen feature, or more correctly the EM, is not affected by particle size, at 1 bar pressure (Cooper et al. 2002 and references therein). It should be noted that the EM is clearly seen as a maximum for grain sizes less than 25 μm or so. For coarser grain sizes it changes to a shoulder which is less diagnostic because the position is less well defined. Significant shift has been found when comparing the wavelength of the EM of solid and powdered samples (Cooper et al. 2002).

Thermal gradients in the sample influence the measured emission spectra in the case of an airless body (e.g., the Moon or Mercury), but not in the case of Mars which has an average atmospheric pressure of about 6 HPa (Henderson and Jakosky 1994, 1997). Detailed studies of heated samples in a vacuum environment and in controlled thermal conditions are badly needed and will be performed in the Emissivity Laboratory in the near future. The spectra will be available in the BED.

Figure 3 shows emission spectra of six plagioclase feldspars for the finest size separates (<25 μm). These minerals are members of the plagioclase solid solution series ranging from sodium-rich end-member albite ($NaAlSi_3O_8$) to calcium-rich end-member anorthite ($CaAl_2Si_2O_8$). As Ca^{2+} cation gradually substitutes for Na^+ in plagioclase structure, structural changes occur which affect frequencies of Si–O vibrations, as well as the related Christiansen frequencies. The spectral changes include a progressive shift of the EM and TM to shorter wave numbers (longer wavelengths) as highlighted by the lines in Fig. 3 which has vertical lines aligned with the position of these features for albite. Changes in relative contrasts of individual RBs are visible, although less pronounced for these spectra of fine-grained samples. The positions of the EM are unaffected by grain size at 1 bar pressure

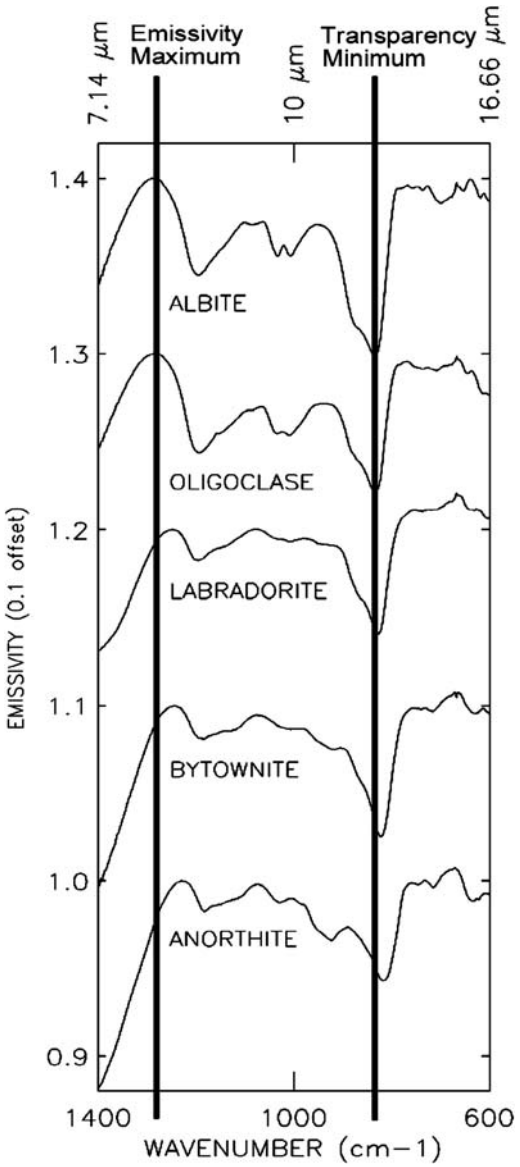

Fig. 3 Emission spectra of five plagioclase feldspars for the <25 μm grain size separate are shown offset for clarity. The trend for the Emissivity Maximum (EM) and the Transparency Minimum (TM) to appear at longer wavelengths as the chemistry changes from Na- and SiO_2-rich to Ca- and with diminished wt% SiO_2 is shown by the *two vertical lines* aligned to the respective features in the Albite spectrum. Data are from the BED (Maturilli et al. 2006a)

(Conel 1969; Cooper et al. 2002) and therefore are highly diagnostic as illustrated by an EM at 7.8 mm (or 1288 cm^{-1}) for albite and at 8.1 mm (or 1234 cm^{-1}) for anorthite.

3.2 Mid-Infrared Studies of Spectral Emissivity from Mercury's Surface

With the availability of sensitive mid-infrared detectors, spectral imaging data acquisition and analysis software, and large telescopes that can be used for daytime viewing when Mercury can be seen from the Earth's surface, a new wavelength region has become available for remotely sensing Mercury's surface composition.

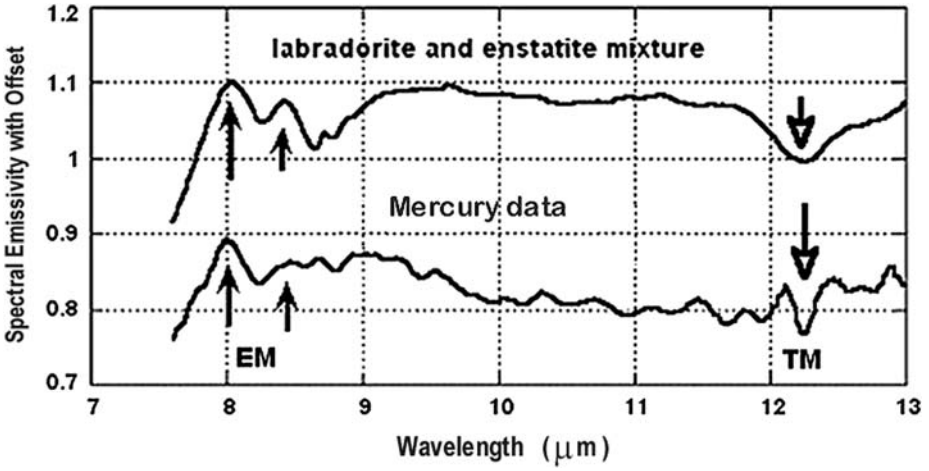

Fig. 4 A spectrum of Mercury's surface from ~240° to 250°E equatorial longitudes shows similarities to a mixture of Na-bearing feldspar (labradorite), and low-iron, Mg-rich orthopyroxene (enstatite). There is a good match at the EM for both minerals and at the transmission minimum (TM) for feldspar. Figure adapted from Sprague and Roush (1998)

Heterogeneous composition of Mercury's surface is indicated by mid-infrared spectra (Sprague et al. 1994, 2002); Sprague and Roush 1998; Emery et al. 1998; Cooper et al. 2001; Donaldson-Hanna et al. 2006). Qualitatively, most spectra match models including plagioclase feldspar and some pyroxene. The common solid solution series of plagioclase feldspar $(Ca,Na)(Al,Si)AlSi_2O_8$ is a strong candidate for a large component of Mercury's surface at several locations as seen in spectra of Figs. 4, 5, 6, 7, 8 and 9. Plagioclase feldspar is formed both at high and low temperatures. Na-rich plagioclase feldspar could have a designation such as $Ab_{95}An_5$ ($Albite_{95}Anorthite_5$) and be comprised of 95% $NaAlSi_3O_8$ (albite) and 5% $CaAlSi_3O_8$ (anorthite). However, as will be shown in the following, spectra from Mercury seem to be better matched by laboratory spectra in the Ab_{50} to Ab_{30} range, roughly labradorite. These spectral signatures may support the suggestion that Mercury has a thick anorthositic crust (Spudis and Guest 1988; Tyler et al. 1988; Sprague et al. 1994; Robinson and Taylor 2001). Members of the pyroxene group are closely related to one another and crystallize in two different systems. The most common orthorhombic pyroxenes are enstatite ($MgSiO_3$) and hypersthene $(Mg,Fe)SiO_3$. The most common monoclinic pyroxenes are monoclinic forms of the common orthorhombic pyroxenes—diopside ($CaMgSi_2O_6$), hedenbergite ($CaFeSi_2O_6$), and augite (intermediate between diopside and hedenbergite with some Al).

Spectral measurements at Mercury from E longitudes 328° to 348°, 316° to 338°, 320° to 315°, 275° to 315°, 316° to 338°, and 240° to 250° are shown in Figs. 4, 5, 6, 7, 8 and 9. The areal extent of the spatial footprint is no smaller than 200 km by 200 km for the very best spatially resolved observations to date (Fig. 9), and as much as 1,000 km by 1,000 km for the least spatially resolved region (Fig. 8). Spectra exhibit emissivity maxima (EM) associated with the principal Christiansen frequency (Sprague et al. 1994; Emery et al. 1998). So far, all EM of spectra from the intercrater plains east of the crater Homer are indicative of intermediate silica content (~50–57% SiO_2). Figure 4 shows one example, a Mercury spectrum from 240°to 250°E longitude compared to a model spectrum created from laboratory spectra of a mixture of plagioclase feldspar and the Mg-rich pyroxene enstatite. Rocks composed of these two minerals might be anorthosite, leucogabbro, or leuconorite.

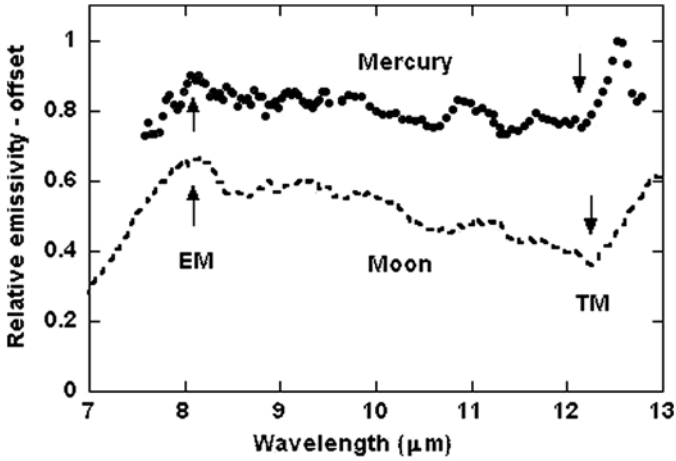

Fig. 5 A spectrum from Mercury's surface (equatorial ~335° to 340°E longitude) is compared with a laboratory spectrum from lunar mission Apollo 16 returned samples (particulate breccia No. 67031: 90% feldspar, 10% pyroxene). Figure courtesy of A.L. Sprague

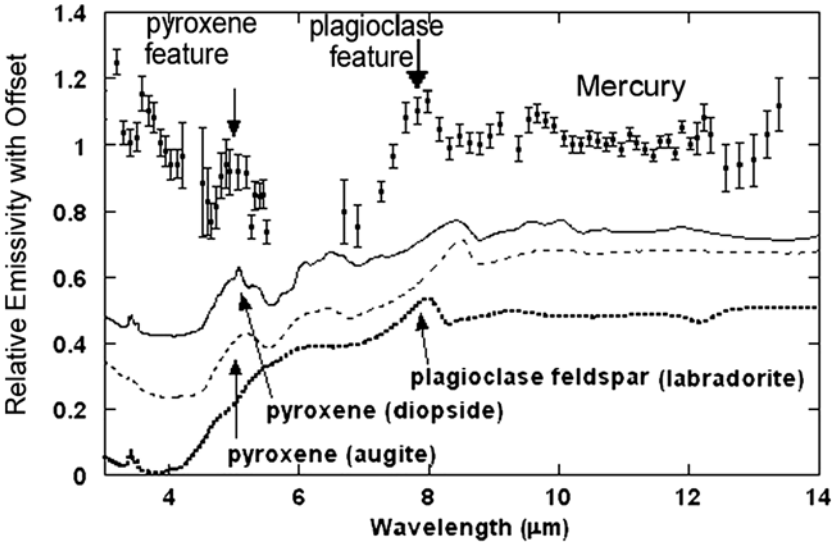

Fig. 6 A Mercury spectrum from the equatorial region of 275° to 315°E exhibits a 5 μm emission feature resembling laboratory spectra of clinopyroxene. The EM at 7.9 μm is indicative of intermediate SiO_2 content and is compared to plagioclase feldspar (Ab_{50}). Laboratory spectra are from Salisbury et al. (1987, 1991). Mercury spectrum is from Sprague et al. (2002)

Figure 5 shows a spectrum from an equatorial E longitudes near 335° to 340° on Mercury's surface and compares it to laboratory spectrum from a particulate breccia sample brought back from the Moon. The number of the sample, No. 67031, indicates that it was obtained at the Apollo 16 landing site. The lunar sample is ~90% anorthite (Ca-feldspar) and ~10% pyroxene. The EM for both spectra is centered close to 8 μm and marked with an arrow. These spectra may indicate the feldspar type on Mercury labradorite rather than

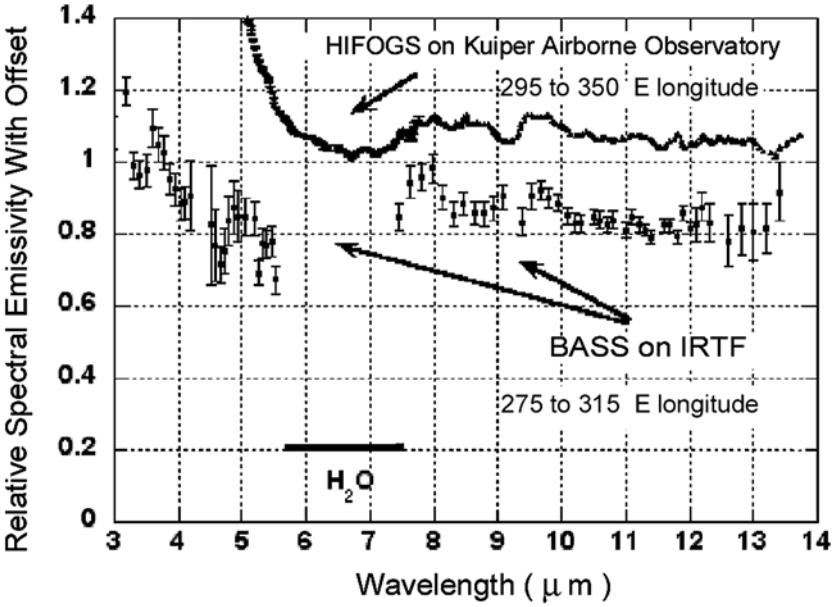

Fig. 7 Two Mercury spectra from adjacent locations on Mercury's surface. In both cases the principal EM is indicative of a feldspathic composition. Other features remain unidentified. Figure is from Sprague et al. (2002)

anorthite which is most common on the Moon. Other features in the Mercury spectrum are also similar to the lunar spectra and likely indicate the presence of pyroxene at this location.

Another spectral feature indicating the presence of clino-pyroxene in Mercury's regolith is a 5 μm emission feature in a spectrum from 275°to 315°E longitude (Fig. 6). The best fit model is to diopside ($CaMgSi_2O_6$). The low-FeO abundance indicated by near-IR reflectance spectroscopy also supports the presence of a low-iron bearing clino-pyroxene. The EM and TM present in the spectrum indicate ∼45% SiO_2 and a mafic bulk composition. Unfortunately, the two pieces of information (pyroxene and weight %SiO_2) are not enough to uniquely identify the rocks that formed the regolith at this location. Powders of either low-iron basalt or anorthosite with about 90% plagioclase and 10% low-iron pyroxene could give the same features.

Based on the spectra shown in Figs. 4, 5, 6, 7, 8 and 9, it appears that Mercury's regolith has a high concentration of plagioclase feldspar, perhaps labradorite $(Na,Ca)Si_3O_8$. An alternative explanation for the apparent match to plagioclase feldspar is that the spectrum comes from the glassy soil on Mercury's surface that is very mature after aeons of meteoritic bombardment. Scientists have shown that if lunar soils are very mature, much of the FeO is removed from the glasses and they appear much more feldspathic in laboratory spectral measurements (e.g., Hapke 2001). However, the microwave observations show Mercury's regolith to be very transparent relative to the Moon so the elemental iron component cannot be very large (Mitchell and de Pater 1994).

A spectrum obtained using the High Resolution Faint Object Grating Spectrometer (HIFOGS) from the Kuiper Airborne Observatory (KAO) which flew at 35,000 ft., above much of the Earth's attenuating atmosphere (Fig. 7) has multiple EMs indicating a complicated bulk composition and or mixed mineralogy at 200° to 260°E (Emery et al. 1998). The spectrum from Fig. 6 is plotted again with the HIFOGS spectrum in Fig. 7 for comparison. While

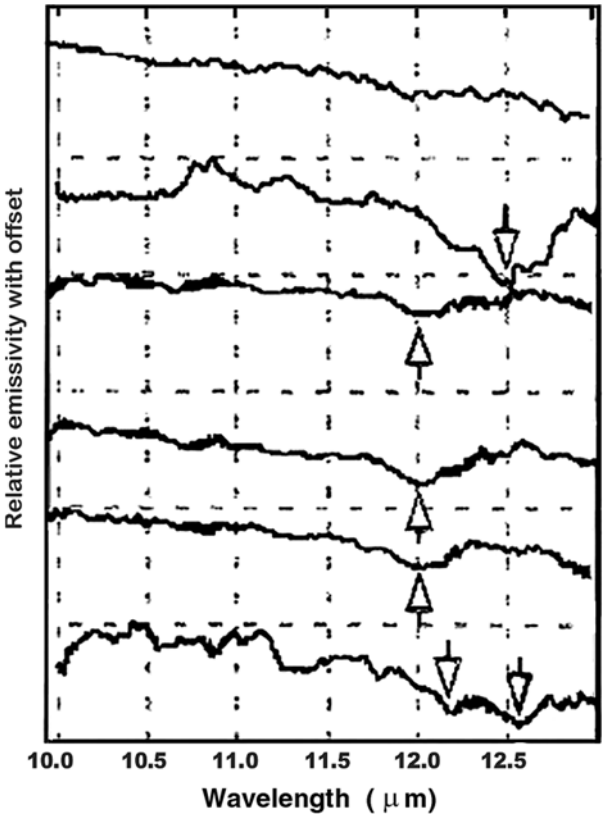

Fig. 8 Spectra from Mercury's surface at six different locations show transparency minima (TM). Sub-Earth and sub-solar longitudes are given in the text. Wavelengths of TM are between 12 and 12.7 μm. Locations (spanning tens of degrees of longitude and equatorial latitude) are estimated from simple thermal models and centered at: from top to bottom, ~280°, 275°, 180°, 170°, 350°, and 215°E. Spectra are from Cooper et al. (2001)

some spectral features appear to be repeated, more observations and modeling are required to make compositional identifications.

Figure 8 shows spectra exhibiting transparency minima (TM) measured from the McMath Pierce Solar telescope on Kitt Peak. A circular aperture was placed over the entire Earth-facing disk of Mercury on six different days. The spectral signature comes from the hottest regions in the field of view. For the spectra shown (top to bottom in the figure), subsolar longitudes are 280°, 275°, 180°, 170°, 350°, and 215°E, respectively. The sub-Earth longitudes on Mercury for the days of observation are: 350°, 345°, 104°, 94°, 280°, 131°E, respectively, and are the E longitude equivalent of the W longitudes given by Cooper et al. (2001). Wavelengths of the TM are between 12 and 12.7 μm. A simple model gives an estimate of the longitude responsible for the greatest flux at the detector. Spectra from ~180°, 170°, and 350°E longitude (3rd, 4th, and 5th from top) have probable transparency minima at 12 μm. The bulk composition associated with a transparency feature at this wavelength is intermediate to basic (45–57 wt%SiO_2). The spectrum from ~275°E (2nd from top) has a TM at 12.5 μm indicative of about 44 wt %SiO_2 or an ultra-basic composition. The spectrum (6th from the top) from ~215°E longitude has a doublet TM indicating two different dominant components in the regolith, one mafic and one ultra-mafic. For comparison, the Mercury spectrum from 240°to 250°E longitude (Fig. 3) has a clear and strong TM at 12.3 μm that is at the same location as the TM in a laboratory spectrum of labradorite powders.

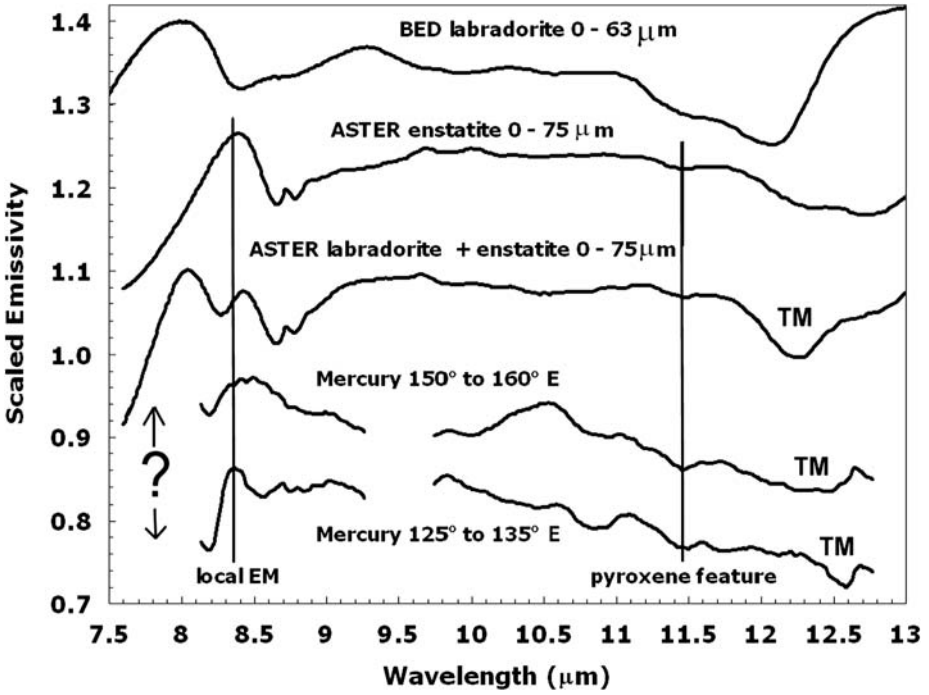

Fig. 9 Three laboratory spectra are plotted along with two spectra from Mercury's surface on the same wavelength scale. All spectra have been offset to distinguish similarities and differences. The *?* indicates no data are available. From top to bottom: true emissivity spectrum of fine-grained (0–63 μm) labradorite (Ab_{50} to Ab_{30}) from the BED, enstatite.1F ($MgSiO_3$) reflectance spectrum, converted to emissivity using Kirchoff's relation, $E = 1 - R$ (Salisbury et al. 1991 and the ASTER data base; grain size 0 to 75 μm), model spectrum computed by linear mixing enstatite.1F ($MgSiO_3$) and labradorite.1F (Ab_{50} to Ab_{30}); grain size 0 to 75 μm, Mercury: region from Caloris Basin, Mercury: region west of Caloris Basin

Laboratory spectra of plagioclase feldspar (labradorite), pyroxene (enstatite), and a mixture of albite and enstatite are shown in Fig. 9 along with two Mercury spectra obtained April 7, 2006, at the NASA Infrared Telescope Facility (IRTF) using the Mid-InfraRed Spectrometer and Imager (MIRSI). The laboratory spectra span from 7.5 to 13.0 μm and thus exhibit the principal EM characteristic of feldspars between 7.5 and 8 μm. The Mercury spectra from Caloris Basin (150° to 160°E) and somewhat to the west of Caloris Basin (125° to 135°E) do not cover the 7.5 to 8.2 μm because MIRSI is not currently configured to permit measurements in that spectral region. Spectral features indicative of Mg-rich orthopyroxene (enstatite) are observed. Very suggestive are the local EM near 8.35 μm, a small emittance peak at 8.72 μm, and a local minimum centered at 11.45 μm as shown in Fig. 9.

Mafic spectral features are indicative of rocks that include olivine and pyroxene in their chemistry or are under-saturated in SiO_2(feldspathoids). Spectral features indicative of clinopyroxene are apparent in ground-based spectra as discussed previously and shown in Figs. 1 (near-IR), 6, and 7. Orthopyroxene (enstatite) is indicated at other longitudes (Fig. 9). Olivine $(Mg,Fe)_2SiO_4$ forms a continuous solid solution of two end member components, Mg_2SiO_4 (forsterite) and Fe_2SiO_4 (fayalite). The low-iron end-member, Mg-rich variety, is a good candidate for Mercury because rocks of this type would not exhibit a strong FeO absorption band in their near-IR spectra. Picrite and dunite are olivine-rich, low-SiO_2 rocks. Tephrites have little olivine while basanites may have considerable olivine but

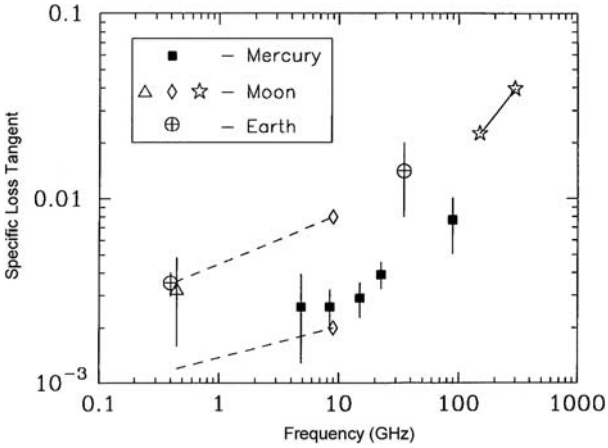

Fig. 10 Ground-based microwave imaging and modeling determined the specific loss tangent of materials in Mercury's regolith and found them to be systematically lower than those of the Moon and a suite of terrestrial basalts (Mitchell and de Pater 1994). *Solid and dashed lines* connect measurements made of the same sample at both 45 MHz and 9 GHz. The inference is that Ti and Fe are not as plentiful on Mercury's surface as on the Moon and that Mercury is not likely to have iron- or titanium-bearing basalt on its surface

both have $Na_2O + K_2O$ of 3 to 9 wt%. Feldspathoids like nepheline syenite are low in SiO_2 (<41 wt%) and have been suggested for Mercury on the basis of trends in some spectral data (cf. Sprague et al. 1994; Jeanloz et al. 1995 and Emery et al. 1998).

On the Moon, lava flows are mostly Fe- and/or Ti-bearing basalts. On Mercury there is little evidence for the Fe-bearing basalts or TiO_2 in significant abundance. Microwave observations and near-IR spectral modeling and comparisons to the Moon appear to rule them both out. In at least two cases the smooth plains overlie material that is bluer (higher UV/orange ratio) and enriched in opaque minerals relative to the hemispheric average (Robinson and Lucey 1997). An estimate of the FeO content of the mantle can be made as follows. Since the smooth plains are probably lava flows, and the FeO solid/liquid distribution coefficient is about 1 during partial melting, it is estimated that Mercury's mantle has a FeO content similar to lava flows and is <3%.

4 Microwave Emissivity of Mercury's Surface

The previous section shows how visible and near infrared spectral studies seem to indicate that there is no or little evidence for the Fe^{2+} charge exchange absorption band in Mercury's regolith. These observations do not preclude iron in nanophase particles or in sulfides. More ground-based observations may yet find some evidence for these. However, detailed measurements of Mercury's regolith from 0.3 to 20.5 cm wavelength indicate that Mercury's surface is more transparent to electromagnetic radiation at these wavelengths than the lunar surface and a suite of terrestrial basalts. These measurements demonstrated that Mercury's surface materials differ from those of the Moon by being significantly lower in materials opaque to electromagnetic radiation such as FeO and TiO_2, and the rocks and minerals containing them (Mitchell and de Pater 1994). This relationship is illustrated in Fig. 10, where the specific loss tangents as a function of frequency of Mercury's regolith are shown compared to those from samples of lunar maria, highlands, and terrestrial basalts.

5 What is the Expected Crustal Composition of Mercury?

The small number of papers that have been able to model the composition of Mercury (Mitchell and de Pater 1994; Sprague et al. 1994; Blewett et al. 1997; Emery et al. 1998;

Table 1 Oxide abundances (wt%) of bulk Mercury according to formation model

MC	ERR	Preferred	EVR	OC
Al_2O_3	16.6	3.5–7	3.3	
CaO	15.2	2.5–7	3.0	Some (in exosphere)
TiO_2	0.7	0.15–0.3	0.14	$\ll 1$ (>0)
MgO	34.6	32–38	32.1	
SiO_2	32.6	38–48	45.0	39–57
FeO	0	0.5–5	15.1	<3 (0.5–2)
Na_2O	0	0.2–1	1.4	Much? (in exosphere)
H_2O	0	Little	Much	Buried at poles? (late meteoritic)

MC = mantle crust system (bulk silicate fraction),
ERR = extremely refractory-rich,
EVR = extremely volatile-rich,
OC = observational constraints on oxide abundances

Sprague and Roush 1998; Sprague et al. 2002; Warell and Blewett 2004: Warell et al. 2006) give only rough bounds on the surface chemistry. Mid-infrared thermal emittance spectroscopy is particularly important with its potential to identify the presence of a range of rock types, specifically those which are iron-poor or iron-free which and are altered by space weathering processes.

5.1 Our Best Guess Models

The summary of present abundance estimates are not yet adequate to constrain Mercury's formation model. The details are given in Table 1 where the bulk content of oxide abundances in wt% for Mercury are shown according to formation model. The first four columns are from Goettel (1988). Observed abundance data are taken from Warell and Blewett (2004), Cooper et al. (2001), Sprague et al. (1998, 2002), Mitchell and de Pater (1994), Blewett et al. (1997), Moses et al. (1999), and Butler et al. 1993.

The extreme end-member models, with high abundances of either refractories or volatiles, are unlikely to have occurred because the circumstances leading to such compositions are highly restrictive. In the preferred model of Goettel (1988) the pure refractories (Al, Ca, Ti oxides) are fully condensed and thus not fractionated with respect to each other. They are moderately enriched above solar (chondritic) values because of accretion within the planetary feeding zone of some material in which Mg silicates were only partially condensed. The magnesium to silica ratio Mg/Si is greater than solar as Mg was enriched relative to pure refractories and thus depleted in Si. Most material, however, accreted from the region where both Mg and Si were fully condensed, and thus Mg/Si is close to the solar value. Significant amounts of (moderately) volatile components (alkalis, FeO, FeS, water) are predicted and are strongly dependent on the extent of the feeding zone. It is postulated that the Fe/Si bulk value of Mercury was increased following initial planetesimal accretion and differentiation by processes operating independently of composition of silicate component. Such processes might be aerodynamic fractionation (in the planetary nebula, larger, denser material is more subject to drag forces than smaller, less dense material) or giant impact(s).

The oxide abundances indicated by the available observations conform to those predicted by the preferred model, except perhaps for the high range of Si inferred from the measurements. However, none of the suggested formation models can be singled out as more or less

likely. In terms of FeO, which is the only oxide for which the abundance has been possible to model based on VISNIR spectra, a bulk weight fraction of 1–2% is consistent with models predicting wide accretion zones (Goettel 1988; Lewis 1988; Wetherill 1988) and models with fractionation processes linked to preferential accretion of metal (0.5–6 wt%; Weidenschilling 1978). The value is greater than or equal to those predicted from the vapor fractionation model (0–3 wt%; Fegley and Cameron 1987), and compatible with mantle-stripping by late-stage giant impact (Benz et al. 1988). Not even the pure equilibrium condensation model (Lewis 1972) predicting zero FeO can presently be discarded on observational grounds, as the native crustal composition may have been fully iron-free and the iron contributed by chondritic infall.

Given these caveats, Mercury's surface appears to be heterogeneous in composition, trending toward feldspar with moderate Ca and Na. There may be feldspathoidal-rich terrains. Some mafic and ultra-mafic minerals such as clinopyroxene have been indicated by spectroscopy and olivine is likely present, but of the Mg-rich, low-Fe variety. None of the observations so far contradict the scenario of early core formation accompanied by contraction of the planet and retention of internal heat through closing off magma vents to the deep mantle (Solomon 1977; Jeanloz et al. 1995). Magma from the deep mantle would presumably be Fe-rich, which is contradictory to the spectral evidence from Mercury's surface.

Based on morphological and spectral observations, extrusive lavas are probably on the surface (Robinson and Taylor 2001; Strom and Sprague 2003), but it appears they may trend toward feldspathoids, alkali-rich alumino silicates with low (39–45 weight%) SiO_2 like tephrite or basanite (Jeanloz et al. 1995; Emery et al. 1998) and be enriched in Na, and possibly K. Such rocks are formed from plagioclase bearing lavas in which feldspathoids are present in greater abundance than 10 wt%.

A relatively large abundance of K in Mercury's exosphere has been reported over the longitude of Caloris Basin roughly in the mid-latitudes (Sprague et al. 1990). The K could be from impact melt associated with the impact that formed the basin, or from an episode of low temperature extrusive volcanism induced by the Caloris impact event. A well-developed fracture system in the basin may have K-rich minerals and serve to conduit K to the exosphere. This speculation requires testing by MESSENGER and Bepi Colombo.

Expansive regions near Homer and the Murasaki Crater Complex (315° to 330°E) appear feldspathic (Robinson and Taylor 2001), trending toward Ab70–Ab40, more Na-rich than the lunar anorthosites (Sprague et al. 1994). Bulk compositions are of intermediate silica content. Some mixed compositions of more basic silica content are present in equatorial longitudes from 200° to 292°E. Two candidates for the rocks at these locations are Na-rich anorthosites. Another possibility is low-Fe basalt, a rock with mixtures dominated by feldspar, minor pyroxene and olivine with a bulk rock chemistry of intermediate (52–57 wt% SiO_2) or mafic (46–51 wt% SiO_2) composition.

6 Augmenting Current Knowledge with Instrumentation on MESSSENGER and Bepi Colombo

The prospects of determining the bulk crustal composition and mode of formation will be very difficult or impossible with ground-based data. These issues will, we hope, be resolved with close-range spectroscopy and imaging with the upcoming orbiters, with information from the smallest resolvable scales (<10 m) playing a critical role in determining the composition of individual or clustered crystalline rocks or rock outcrops. Almost all of the observations have also raised new questions to be answered by the suite of instruments on the

MESSENGER spacecraft, scheduled to begin mapping Mercury's surface in 2011 (Solomon et al. 2001; Gold et al. 2001; Santo et al. 2001).

The ESA mission, Bepi Colombo, scheduled for launch in 2011, has instrumentation ideally suited to making surface composition measurements. If all goes as planned, those measurements will test the conclusions that have been presented above in this section. The MERTIS instrument is an IR-imaging spectrometer based on the pushbroom principle (Benkhoff et al. 2006). MERTIS uses a micro-bolometer detector which requires no cryogenic cooling and which makes it ideally suited for the hot environment around Mercury. MERTIS has an integrated instruments approach which will allow including a so-called μ-radiometer by sharing the optical entrance path, instrument electronics, and in-flight calibration components. The μ-radiometer uses highly miniaturized thermopile detectors and will be placed at the slit of the spectrometer.

MERTIS covers the spectral range from 7–14 μm at a high spectral resolution of up to 90 nm which can be adapted even along an orbital track, depending on the actual surface properties to optimize the S/N ratio. With this spectral coverage and resolution MERTIS will be able to detect the main features in this spectral region, such as the Christiansen wavelengths (emissivity maxima), the emissivity minima in the Reststrahlen region and the transparency features (Helbert et al. 2007).

MERTIS will globally map the planet with a spatial resolution of 500 m and a S/N of at least 100. For a typical dayside observation the S/N ratio will exceed 1,000 even for a fine-grained and partly glassy regolith. MERTIS will map 5–10% of the surface with a spatial resolution higher than 500 m. The flexibility of the instrumental setup will allow study of the composition of the radar bright polar deposits with a S/N ratio of >50 for an assumed surface temperature of 200 K. Depending on the exact orbit and therefore the distance from Mercury's polar regions, the spatial resolution could be as good as 1–2 km. In addition, by integration of the μ-radiometer MERTIS will be able to measure thermophysical properties of the surface like thermal inertia and internal heat flux and derive from this further information on surface texture and structure.

Another instrument that will be important for the study of Mercury's surface is the stereo camera (a channel of SIMBIOSYS—one of the payload instruments on board the Mercury Planetary Orbiter) of Bepi Colombo. It will perform 3-D global mapping of Mercury's entire surface and make multi-colored maps with a scale factor of 50 m/pixel at the periherm (400 km above the surface). It will allow the cataloging of the Digital Terrain Model of the entire surface and dramatically improve the interpretation of morphological features at different scales and topographic relationships.

The harsh environment of Mercury will strongly affect the functionalities and performance of the instruments, and even for the stereo camera we had to find a new solution and a new technique of acquiring the stereo pairs for generating the Digital Terrain Model of the surface. The instrument concept is based on an original optical design composed by two channels, looking at the surface at $\pm 20°$ from the nadir direction, converging on the same bidimensional focal plane assembly, with no mechanism (Da Deppo et al. 2006). The configuration of the focal plane assembly allows to apply the push-frame technique to acquire the stereo images, instead of the push-broom usually used by other planetary and terrestrial stereo imagers.

7 Space Weathering and Surface Maturation

Although the remote-sensing spectroscopic studies of Mercury are important, the results must be viewed in context of the exceptionally dynamic environment of the inner solar sys-

tem. Space weathering processes and the contribution of exogenic chondritic material (see, e.g., Hapke 2001, 2007, this chapter; Langevin and Arnold 1977; Langevin 1997; Lewis 1988; Cintala 1992; Noble and Pieters 2003) strongly affect the chemistry and observed properties of the mercurian surface. Thus, no interpretation of the composition of Mercury's true crustal composition can be made without thoroughly accounting for space weathering, maturation and exogenic deposition on its surface.

According to the general maturation model, the VISNIR spectral properties of the regolith of an atmosphereless mafic silicate body are governed by three major components (Hapke et al. 1975; Rava and Hapke 1987: Hapke 2001): (1) ferrous iron as FeO in mafic minerals and glasses, increased abundance increases the depth of the near-infrared Fe^{2+} crystal field absorption band; (2) nm-sized $npFe^0$ particles formed by vapor deposition reduction in rims of mafic grains, increased abundance decreases the reflectance and increases the spectral slope ("reddening"); (3) spectrally neutral Ti-rich opaque phases such as ilmenite in minerals and glasses, increased abundance decreases the reflectance but decreases the spectral slope. The mean grain size is also a critical parameter for interpreting surface spectra, as band depths and band shapes strongly depend on this parameter for a given mineralogical composition. Nanophase metallic iron ($npFe^0$) is formed during the maturation process due to micrometeorite impacts and solar wind sputtering of the surface. The process is caused by condensation of Fe-bearing silicate vapors in silicate grain rims by selective loss of oxygen (Hapke et al. 1975; Hapke 2001 and references therein). Very small abundances of metallic iron as $npFe^0$ have drastic effects on VISNIR spectral shape and reflectance and must be understood and calibrated out of observed spectra in order to derive the composition of the unweathered material.

As discussed by Langevin and Arnold (1977) for the lunar regolith, maturity on an airless body such as the Moon or Mercury results from a competition between macroscopic gardening, which brings fresh material from the bedrock to the surface, and the space weathering processes which occur at or very close to the surface. The thickness of the debris layer (or regolith) grows as a function of time as new material is excavated. Over the last 4 billion years, the impact rate is expected to have remained stable, as it results from a steady state transfer of impactors close to resonances in the main belt (see e.g. Marchi et al. 2005). On the Moon, the mean regolith accumulation rate during this period has been in the range of 1 m/by, as demonstrated by the radiation exposure ages of deep-drill lunar cores. Given the stochastic nature of meteoroid bombardment, a soil sample can stay exposed at the surface for millions of years, then be covered by a new ejecta blanket, possibly to be exposed again several hundred million years later by an impact in the regolith. Nevertheless, the mean amount of time a given volume element of regolith spends within 1 mm of the surface on the Moon has to be close to 1 my. This mean residence time is controlled by the flux and velocity of large impactors which are able to dig down into the bedrock (size range of 1 m or more).

Freshly excavated ("immature") material is initially coarse grained (from the mm range to rocks, even m-sized boulders) and dominated by crystalline grains. A wide variety of space weathering processes modify the size distribution, mineralogy, and optical properties of the constituents of the regolith. A direct micrometeoroid impact can result either in a microcrater (if the grain is large) or in fragmentation. Conversely, macroscopic and microscopic impacts generate fused silicate droplets which can either solidify in flight (forming glass spherules) or weld together crystalline grains (forming glassy agglutinates). Eventually, a steady state grain size distribution is reached with a median size of $\sim$50 μm. The fraction of glassy material can reach 50% or more in highly mature lunar soil samples which have accumulated a lot of surface residence time. Nanophase metallic iron is formed during

the maturation process due to micrometeorite impacts and solar wind sputtering of the surface. Other maturity effects such as the formation of particle tracks within the grains due to heavy ions in cosmic rays play a relatively minor role for optical and spectral properties.

Therefore, the most important space weathering parameters are the micrometeoroid flux (masses <1 mg) and velocity (which controls the production of glass and the fragmentation efficiency) and the flux of low-energy ions (solar wind or magnetospheric precipitation). When trying to assess the maturity state on Mercury, one has to assess these space-weathering factors as compared to the mean residence time of the surface which is controlled by large scale impacts. The well-documented situation on the Moon can then be considered as a reference case. This can be done on much firmer ground than in 1996 (date of the first Mercury workshop in London) as there are now reliable models of the relative impact rates on inner planets for various populations of meteoroids injected by resonances in the inner solar system. Marchi et al. (2005) concluded that the flux of large impactors on Mercury is one-tenth of that on the Earth. If one considers gravitational focusing, which enhances the impact rate on the Earth by a factor of 1.4, and the factor of 7 between the surfaces, the flux of large impactors per surface element, which controls regolith formation, is expected to have been similar on Mercury and on the Moon during the last 4 billion years. According to Marchi et al. (2005), there is a significant difference in terms of mean impact velocity (30 km/s on Mercury, 20 km s^{-1} at 1 AU). This will result in a cratering efficiency increase by a factor of 1.5 to 2. The mean rate of regolith formation on Mercury could therefore range from 1.5 m per by to 2 m per by.

One can expect a much higher flux of low-energy ions at 0.3 AU when compared to the Moon at 1 AU, even if the situation is made more complex by the shielding effect of Mercury's magnetosphere. The radial dependence of micrometeoroid fluxes is different from that of large-sized meteoroids, as the latter are dominated by asteroidal contributions while the small size range is much more complex (e.g. Divine 1993), with a large contribution of cometary material and zodiacal dust. From the evaluations of Müller et al. (2002), the dust flux near Mercury is enhanced by a factor of 1.5 to 3 when compared to that on the Moon. The impact velocity of the cometary component scale with the local orbital velocity, hence the available energy per dust impact is increased by a factor of $\sim$2.5 when compared to the lunar situation, with wide variations as a function of the true anomaly. The space-weathering efficiency of micrometeroids should therefore be 4 to 7.5 times higher on Mercury than on the Moon. The comparison between this factor and the factor of 1.5 to 2 between regolith accumulation rates suggests that the mean integrated maturity indices in the regolith of Mercury are at least twice higher than it would be in the lunar regolith. These new evaluations are therefore consistent with the conclusions of Langevin (1997).

Unlike at the Moon, the situation on Mercury is by no means equivalent for all surface elements. The solar wind sputtering flux is controlled by the 3 : 2 spin–orbit coupling, which causes an uneven irradiation pattern which is further modulated by magnetospheric screening and precipitation. Minor effects are implantation of solar wind species (C, N, H), and major effects include amorphication and/or chemical reduction of the outer rims of grains. The solar photon flux is also controlled by the spin–orbit coupling, and at the highest surface temperatures the effect is thermal annealing of radiation damage effects and an increase in $npFe^0$ particle size because of Ostwald ripening. Furthermore, impact velocities and rates are expected to strongly depend on true anomaly. Orbiter missions to Mercury may well reveal variations of the mean maturity indices between the two antipodal longitudes which are subsolar at perihelion and the intermediate longitudes which are subsolar at aphelion.

8 Exogenic Material from Comets, Meteorites and Interplanetary Dust Particles

8.1 Sungrazing Comets

Sungrazing comets have been observed for many hundreds of years. In the late 1880s and early 1890s, Heinrich Kreutz studied the possible sungrazing comets which had been observed and determined that some were sungrazers and some were not. He also found that those which were indeed sungrazers all followed the same orbit. That is, they were all fragments of a single comet which had broken up. It is probable that the original comet, and its fragments, have broken up repeatedly as they orbit the sun for a period of about 800 years. In honor of his work, this group of comets is named the *Kreutz sungrazers*. The Kreutz sungrazers come within about 50,000 km (perihelion distance of 0.005 AU) of the solar surface.

Beginning in 1979, coronagraphic observations from space allowed the detection of numerous additional Kreutz members that were completely vaporized as they grazed the Sun. Since 1996, the Solar and Heliospheric Observatory (SOHO) coronagraphs have revealed some 700 of these comets. This suggests that there is a constant stream of small members and that the break up occurred quite recently near aphelion. Break-up near perihelion requires that the observed dispersion of the orbital parameters would take many millennia. However, recent calculations have shown that the evolution can be substantially sped up by allowing fragments to be rotationally spun off at heliocentric distances of many tens of AU. Since the turn on of the LASCO instrument on December 30, 1995, through September, 2006, it has discovered 1,185 new comets of which about 8% belong to the Kreutz sungrazing group. The majority of the remaining comets belong to three new groups—the Meyer (5%), Marsden (2%), and Kracht (3%) groups—that were declared based solely on LASCO comet observations.

All the observed comets have clearly been very small, and the data suggest that few survived perihelion passage in any coherent fashion. The brightness distributions of the Kreutz comets detected with SOHO/LASCO indicate an increasing number of comets with decreasing size and the size distribution of nuclei is probably described with a power law. Based on a much smaller sample, observed from the end of 1996 until the end of 1998, Sekanina (2003) gave an apparition rate of 0.6 per Earth day. Then he estimated from his model that the initial diameters of SOHO sungrazers range from 17 to 200 m yielding the total mass of incoming comets of $M = 2 \times 10^{12}$ g arrived during the ~2 Earth years long interval, equivalent to 3.1×10^4 g s^{-1}.

Mann et al. (2005) tried to estimate the dust supply from the sungrazers assuming a spherical comet of 20-m radius fragmented into 10 μm spherical particles and distributed in a sphere of 10 solar radii. They found a number density of 10–17 cm^{-3}, which is below typical densities of 10–14 cm^{-3} for particles of this size range. They assumed this large size of dust grains, since for size distributions that are similar to that in the interplanetary dust cloud, the majority of mass would be contained in fragments of this size. Analysis of the dust tails of sungrazing comets shows that the sungrazers emit small particles of sizes $a = 0.1$ μm and that the dust in the sungrazing comets has a narrow size distribution (Sekanina 2000). When making this rough estimate for 0.1 μm spherical particles, the number density amounts to 10–12 cm^{-3}, which is comparable to typical dust densities in this size range. Moreover, the dust that is produced by sungrazers will quickly leave the solar corona. The Kreutz comets are in highly elliptic or hyperbolic orbits, their speed is approximately 230 km s^{-1} at 7 solar radii and can be described as bodies with initial speeds of zero at infinity that fall into the Sun. Dust grains released from the sungrazers are in similar orbits.

Furthermore, the perihelion distances and inclinations of the other three groups of sungrazers are 0.036 AU and 72.4°, 0.049 AU and 27.4°, and 0.048 AU and 13.6°, respectively, where each value is the mean weighted by the total observational time (Meyer 2003). The size of these comets is likely to be similar to the Kreutz family fragments SOHO detects, but because of the larger perihelion distances, the smallest members of the groups are probably not detected. The apparition rates of these comet groups and therefore the input to the near-solar dust cloud are clearly below those of the Kreutz group comets.

Mann et al. (2005) concluded that the dust supply from the frequently observed sungrazing comets is negligible, but they did not have a complete dynamical model of small particles released by these objects that may supply a large amount of dust. Considering that we do not have the size distribution released by the sungrazers, we cannot obtain a good estimate of the dust supply in the inner Solar System, and the particles smaller than 1 cm seems to be important for the Mercury's exosphere (Cremonese et al. 2005).

The dust supply from larger comets near the Sun can produce dust density enhancements that are comparable to the dust densities in the solar environment (Mann et al. 2000). The dust density may be raised many fold over a time span of weeks. Such relatively lower probability events are important for providing volatiles to the inner solar system.

As dynamical information on the sungrazers and their dust size distribution and production becomes better understood, we can apply this knowledge to how much dust is contributed to Mercury's surface and predict the depth to which the surface reflects more the exogenic source than the native crustal composition.

8.2 Meteoroids

In this section we report an estimate of the mass of meteoroids that has impacted the entire surface of Mercury during the last 3.8 Gy (from the end of the Late Heavy Bombardment to present). The calculations were performed using the model of Cremonese et al. (2005) and Bruno et al. (2006) in the size range of 10^{-8}–10^{2} m radius. The size range has been limited to a radius of 100 m, since the differential velocity distribution of the meteoroids was determined by Marchi et al. (2005) only for 10^{-2}–10^{2} m radius objects.

In the last 3.8 Gy the mass of meteoroids that has impacted the whole surface of Mercury has been 8.86×10^{18} and 2.66×10^{19} g, respectively. Only 2% of the mass comes from meteoroids with radius 10^{-2}–10^{2} m. This is a rough estimate of the meteoroids' mass, obtained not considering the flux of objects with radius larger than 100 m and assuming a constant flux of the meteoroids with radius $\leq$100 m during all the 3.8 Gy. In any case, this estimate allows us to consider the variation of Mercury's surface composition owing to the contribution of meteoritic material. For the sake of simplicity, Bruno et al. (2006) assumed that their composition, for all the size range considered in their work, is equal to that of the S-type igneous asteroids (e.g., Krasinsky et al. 2002), which are the main constituents of the inner part of the Main Belt. In these rocks the olivine is the most abundant mineral (its composition varies from 0 to ~30 mol.% Fe_2SiO_4), with subordinate amounts of low-Ca pyroxene, nickel-iron and troilite, and minor sodic plagioclase and diopside; the Fe contents ranges from ~18 wt% to ~30 wt%, the Ca content is of the order of ~1–2 wt%, and the Na and K contents are ~0.3–0.6 and 0.05–0.1 wt%, respectively (e.g., Dodd 1981).

Considering such meteoroids composition, Bruno et al. (2006) estimated that in the last 3.8 Gy meteoroids have supplied to Mercury: Fe = (4.79–7.98) $\times 10^{18}$ g, Ca = (2.66–5.32) $\times 10^{17}$ g, Na = 7.98×10^{16}–1.60×10^{17} g and K = (1.33–2.66) $\times 10^{16}$ g. It is clear that a percentage of this material has been ejected in the exosphere consequently to the meteoroid vaporization due to the impact with the planet surface.

Because there is very little evidence for iron on Mercury's surface, either as npFe^0 or as FeO in surface rocks and minerals, the chemical model of Bruno et al. (2006) is not likely to be representative of the actual infalling material. This is an area that requires much more attention.

8.3 Delivery of Solar Material by The Solar Wind

The solar wind flux at the orbit of Mercury is much larger than at Earth orbit, typically about a factor of 10, which is of the order of 4×10^{13} ions m^{-2} s^{-1}. However, since Mercury has a sufficiently strong magnetic field it holds off the solar wind from reaching Mercury's surface most of the time. Since the Mariner 10 flybys through the magnetosphere were on the tail side, the solar wind stand-off distance had to be estimated from the particles and fields data. Early estimates based on scaling the terrestrial magnetosphere gave a stand-off distance of about 1.7 RM (Siscoe and Christopher 1975; Slavin and Holzer 1979). Later, computer modeling of Mercury's magnetosphere allowed more detailed investigations and it became clear that large fractions of Mercury's magnetosphere are open and solar wind ions can access the surface. These open areas are around the cusps and their size and exact location depend on the solar wind plasma parameters, which are mainly the speed, the density, and the magnetic field (Kabin et al. 2000; Sarantos et al. 2001; Kallio and Janhunen 2003; Massetti et al. 2003; Mura et al. 2005). These calculations give precipitating ion fluxes in the range from 108 to 109 cm^{-2} s^{-1} onto the surface at latitudes between 40° and 60° and longitudes ±60° from the subsolar point.

Figure 11 shows a map of precipitating protons calculated for four different cases of solar wind plasma parameters using a hybrid model (Kallio and Janhunen 2003). One can see large areas of proton precipitation in mid latitudes around the cusps (regions are high proton precitation are red, orange). In addition, one recognizes a band (yellow) of precipitation all around the planet arising from magnetospheric ions precipitating onto the surface (auroral precipitation). Again, from these model calculations the precipitating fluxes are in the range from 10^8 to 10^9 cm^{-2} s^{-1} for typical solar wind plasma conditions. The bottom right panel in Fig. 11 shows a situation of a plasma cloud from a coronal mass ejection (CME) interacting with Mercury's magnetosphere. Because of the much larger solar wind dynamic pressure in CME plasmas larger areas at Mercury's surface are open to interplanetary plasma, actually almost the entire dayside of the planet.

We have seen that there are large areas on Mercury's surface that get exposed to solar wind during regular solar wind conditions. Solar wind velocities are in the range of 300 to 800 km s^{-1} (slow and fast solar wind), which translates to energies of 0.5 to 3.3 keV/amu, and with a typical value of 1 keV/amu. In the solar wind, protons and alpha particles make up more than 99% of the ions, and heavy ions (from carbon to iron and up) together are about 0.1% of the solar wind ions in the number flux (Wurz 2005 and references therein). These ions and heavy ions are known to knock atoms bound in the surface regolith free and put them into Mercury's thin atmosphere. This process is called sputtering. For the lunar surface total sputter yields are about 0.07 per impinging ion for the typical mix of solar wind ions (Wurz et al. 2006). Note that the sputter yield is has a maximum around ion energies of 1 keV/amu. Heavier ions have sputter yields even larger than 1, but because their abundance in the solar wind is very low their contribution to the total sputter yield of the solar wind is negligible.

Since the total sputter yield for solar wind is significantly below 1 there is more material transported to Mercury's top-most surface by the solar wind than is sputtered away, and Mercury's surface is expected to be saturated with hydrogen and helium. However, for heavy

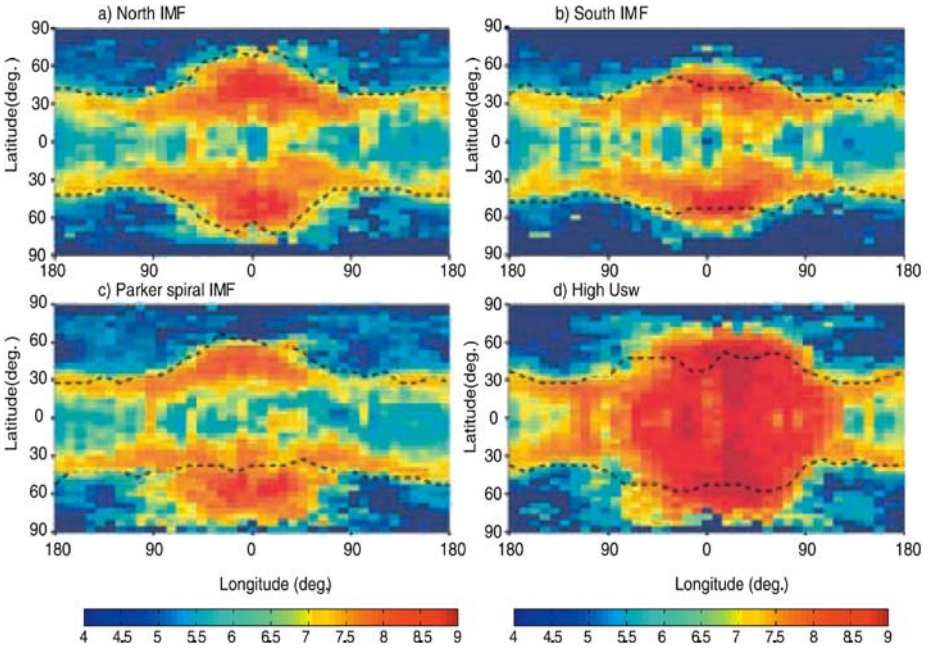

Fig. 11 The particle flux ($cm^{-2}\,s^{-1}$) of impacting H^+ ions (from Kallio and Janhunen 2003). The *dashed lines* show the open/closed field line boundary. The sub-solar point is in the *center of each figure*. The cases are: (**a**) pure northward IMF, (**b**) pure southward IMF, (**c**) Parker spiral IMF, and (**d**) high solar wind speed case (CME type)

atoms (from carbon to iron and up), the removal via sputtering exceeds the input from solar wind by 1 to 3 orders of magnitude depending on species, because the abundance of heavy ions in the solar wind is very low. Since Mercury's gravitational field is low, most of the sputtered atoms escape because their typical ejection speed exceeds Mercury's escape speed of 4250 $m\,s^{-1}$.

Koehn and Sprague (2006) argued that Mercury's surface is likely to be implanted with O and Ca from the solar wind. Using line-of-sight (LOS) O values from (Broadfoot et al. 1976) and an upwardly revised value (Hunten et al. 1988) of 1.0×10^{11} O atoms cm^{-2}, and a rough average of measured LOS Ca abundance (Bida et al. 2000; Killen et al. 2007) of 2×10^8 Ca atoms cm^{-2} gives a Ca/O ratio of 2×10^{-3} with a factor of 2 uncertainty owing to the O measurement and variability of several factors in the Ca measurement. The ratio of Ca/O in the solar wind is 1–4 $\times\ 10^{-3}$ (cf. Wurz et al. 2003, and references therein). The similarity of the Ca/O ratio above the limb of Mercury to the Ca/O ratio in the solar wind compels the serious consideration that a primary source of Ca and O in Mercury's exosphere is the solar wind. If this is true, then spectroscopic measurements of Mercury's surface may be biased by the solar Ca and O abundances. However, within the error bars, using an exospheric surface density for oxygen of $N_O = 4.4 \times 10^4$ cm^{-3} (Hunten et al. 1988), which gives a column density of $N_C = 2.6 \times 10^{11}$ cm^{-2} and a model for thermal release by Wurz and Lammer (2003) and an average of the observed Ca abundance of $N_C = 1.1 \times 10^8$ cm^{-2} (Bida et al. 2000) the solar wind Ca/O ratio is at least a factor of ten larger than Mercury's. More observations of the exosphere are required to determine which scenario is correct.

The main loss process for exospheric atoms, whether they are native to Mercury's crust of recycled from exogenic material, is ionization. Once ionized, exospheric constituents

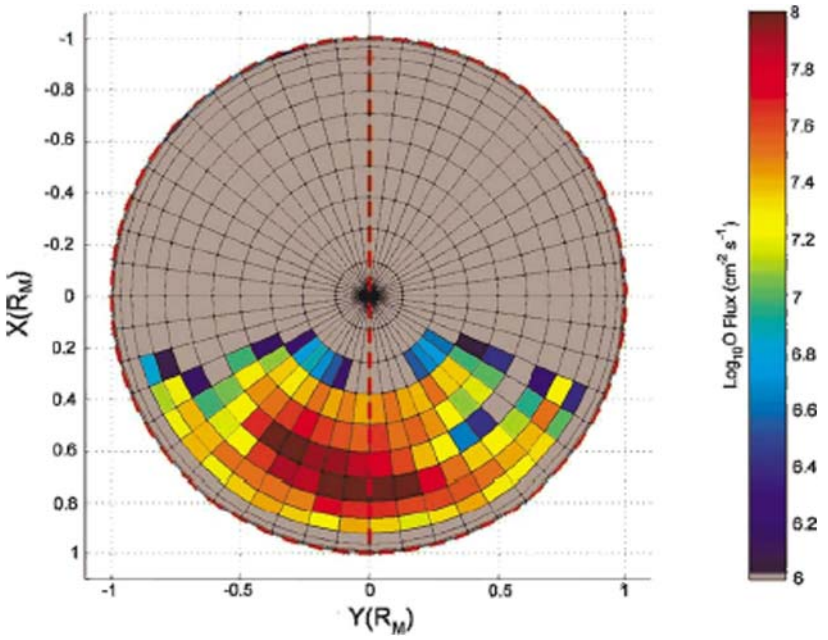

Fig. 12 Color-coded O-ENA flux generated by ion-sputtering on the northern surface of Mercury. Figure is from Mura et al. (2005)

become part of the magnetospheric system of Mercury and some of them are accelerated back to Mercury's surface with energies in the 10 keV range (Delcourt et al. 2003). Preferred places for the precipitation of ions are two belts at $+30°$ and $-30°$ latitude around the planet (the auroral precipitation region; Fig. 11) and the day-night perimeter of the planet (Delcourt et al. 2003). Na^+ fluxes of the order 10^6 cm^{-2} s^{-1} have been calculated for the auroral precipitation region. At these locations one expects enhancements of the top surface in Na and K (Sprague 1992a, 1992b).

Because the amount of exogenically contributed material is not well quantified, it is not possible to determine with certainty if the Ca-rich signatures in Mercury near-IR and mid-IR spectra are native or from a largely exogenic veneer. The search and discovery of true crustal sources of the elements in the exosphere by MESSENGER and Bepi Colombo will help to understand the surface remote sensing data.

9 Exospheric Clues to Surface Composition

9.1 Mercury'S Upper Surface

Mercury's upper surface is probably composed of: (i) interplanetary materials that is, by similarity with Earth's case, meteoritic material, interplanetary dust, and cometary materials; (ii) material originating in the planet's bulk. The relative abundance of these two types of material is unknown. On the basis of existing models, the fraction of meteoritic material is estimated to be in the range from 5–20% to 100% (Bentley et al. 2005) (virtually no release of regolith erosion products in this case). In the second hypothesis, the composition

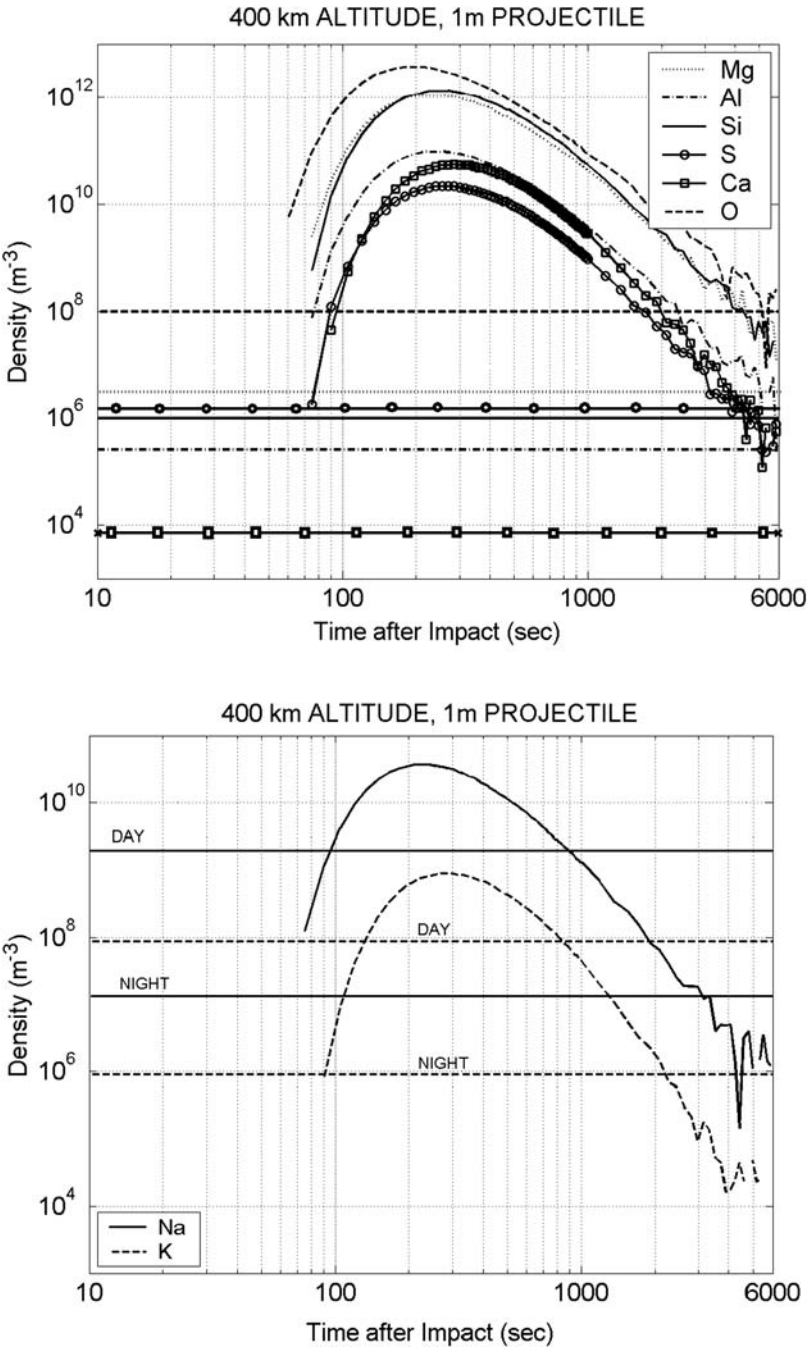

Fig. 13 Density versus time for an impacting object of 1 m radius, at 400 km altitude for the species whose mean density value does not change between day- and night-time (*top*); separately, for Na and K (*bottom*). Horizontal lines represent the exospheric background for each species according to the exospheric model of Wurz and Lammer (2003). Figure is from Mangano et al. (2007)

of Mercury's exosphere reflects the chemical composition of meteorites impacting Mercury, possibly mixed with solar-wind-added products, and no genetic link between regolith and exosphere exists. If only a small fraction of Mercury's exosphere is of meteoritic origin, the remaining comes from the regolith, more precisely from an upper superficial layer, in equilibrium with the exosphere (Killen et al. 2004). The composition of the upper superficial layer, eroded by energetic particles and radiation fluxes, probably significantly differs from the composition of endogenous layers, due to the different extraction rates of the species of different natures, undergoing various extraction mechanisms (Leblanc and Johnson 2003). In a steady state, the net escape fluxes of species at the top of the exosphere are equal to their net extraction fluxes at the surface, which reflect the chemical composition of the unperturbed subjacent regolith. Therefore, the composition of the bulk regolith should be better derived from the total escape rates of atoms and ions (balanced between inflow and outflow in the planet environment).

9.2 Remote Sensing of the Surface Composition Through Exospheric Fluxes

Generally, due to the strong link between the exosphere and the surface, by measuring neutrals and ions at relatively low altitudes it should be possible to get information on the upper surface composition. The subject of exospheric sources and sinks is discussed in detail in "Processes That Promote and Deplete the Exosphere of Mercury" by Killen et al. (2007, this volume). Therefore, we take only a brief visit to this topic.

Some release processes are non-stoichiometric, hence involving only selected species. For example, thermal evaporation and photo-sputtering are more effective for volatiles (like H, He, Na, K, S, Ar, OH). Conversely, ion-sputtering (Killen et al. 2001; Lammer et al. 2003) and impact vaporization (Cintala 1992; Gerasimov et al. 1998) are relatively stoichiometric in releasing species from the surface (also O, Ca, Mg, Si, and other refractory species). Nonetheless, the release efficiency, also for these more stoichiometric processes, depends on the mineralogy (the binding energy of the released atoms), and the altitude profile depends on mass and initial velocity distribution of each species. Therefore, in order to be able to infer a source composition from the in situ exospheric measurements, it is really important to know the mechanism of ejection and the surface properties. Hence, taking into account the effectiveness of the process in ejecting material, information on the surface composition can be deduced; conversely, if we know the upper surface composition, by observing the exosphere composition and the density altitude profiles, information of the active release process can be obtained.

From previous considerations, it follows that the processes that could provide more information on the surface composition are ion-sputtering and micro-meteoroid or meteoroid impact vaporization, since they are able to release the majority of the surface species.

The neutrals released via ion-sputtering can be discriminated from neutral populations released by other processes thanks to their specific characteristics. In fact, this process is highly dependent on local plasma precipitation rate, so that it is confined to a limited area and strongly variable (Kabin et al. 2000; Kallio and Janhunen 2003; Massetti et al. 2003; Mura et al. 2005). Furthermore, the released species are not only volatiles, as mentioned before. Since this process has a wide energy spectrum, that is, it has the bulk of neutral emission in the few eV range, with a not-negligible high-energy tail (hundreds of eV; (Sigmund 1969; Sieveka and Johnson 1984), these neutral atoms can be detected at both lower and higher energies. Finally, the altitude profile related to this process has a higher scale height with respect to other release processes (Mura et al. 2006). Since ion-sputtering also produces a release of charged particles from the surface, the detection of these planetary ions, associated with neutral particle emission, could be a signature of the efficiency of this process.

The micrometeoroid impact vaporization is expected to be the most efficient process in the night side and the only process constantly active over the whole surface of the planet (Killen et al. 2001; Wurz and Lammer 2003). In fact, other generally significant processes, such as ion- and photo-sputtering and thermal desorption, are mainly active in specific regions of the dayside. Anyway, any in situ detection of refractories at energy of a few eV with no signal at higher energies could be the signature of micrometeoroid impact vaporization.

Recently, Mangano et al. (2007) demonstrated that individual impact vaporization events of large meteoroids (about 10 cm or more in radius) on Mercury's surface have a high probability to be observed as elemental enhancements in the planet's exosphere during the Bepi Colombo mission. The material involved by the impact is vaporized within a volume proportional to the meteoroid mass (Cintala 1992). Hence, the analysis of such signals, taking into account the physics of the process and the particle transport in the exosphere, would provide crucial information of the planetary endogenous regolith composition, below the more superficial layers highly modified by space weathering action. In particular, vaporization of >1 m meteoroid impacts (with a frequency of occurrence comparable with the Bepi Colombo mission lifetime) could enrich the exospheric composition with endogenous material released from deeper layers (down to some meters, depending on density and porosity of the regolith). This possible detection could be the only way to obtain remote sensing information about the original composition of the planet surface.

9.3 Is There Enhanced Sodium in the Bright Visible and Radar Albedo Regions Known as Spots A and B?

A curious coincidence of enhanced exospheric Na has been observed at high radar and visible albedo regions (Fig. 14) centered at 25°S, 5°E and 55°N, 5°E, respectively. These have been labeled as spot B (north) and spot A (south) according to the scheme of Harmon (1997). These regions appear as rough in radar backscatter images (cf. Harmon et al. 2007) and presumably are relatively freshly excavated craters. Sprague et al. (1998) discussed several exospheric Na observations of enhanced column abundance over these two regions and Sprague and Massey (2006) showed other ground-based images. The exospheric connection is discussed further in this volume in the chapter by Killen et al. It may be that the crustal materials of Mercury are enhanced in these regions or it may be that the surface materials are enhanced by magnetospheric focusing onto these locations (cf. Potter and Morgan 1990). This puzzle will most likely not be solved until the MESSENGER and Bepi Colombo missions can acquire the data necessary to understand this phenomenon.

10 Radar Observations of Depolarized High Albedo Polar Deposits

The discovery of regions of depolarized radar signals backscattered from deposits near Mercury's north and south polar regions as shown in Fig. 15 (Slade et al. 1992; Harmon and Slade 1992; Butler et al. 1993; Harmon et al. 1994) astounded the planetary science community because the character of the material is similar to the radar backscatter signature from water ice at Mars' summer southern pole and the Galilean satellites. Thermal models (Paige et al. 1992; Butler et al. 1993; Vasavada et al. 1999) and Monte Carlo models of volatile distribution and storage in permanently shadowed regions (Butler 1997; Moses et al. 1999; Crider and Killen 2005) have shown water ice could be stable for a few million years following deposition even with Mercury's proximity to the Sun. It is likely that the stored volatile (if it is a volatile like water ice) is exogenic material from comets, meteorites, and

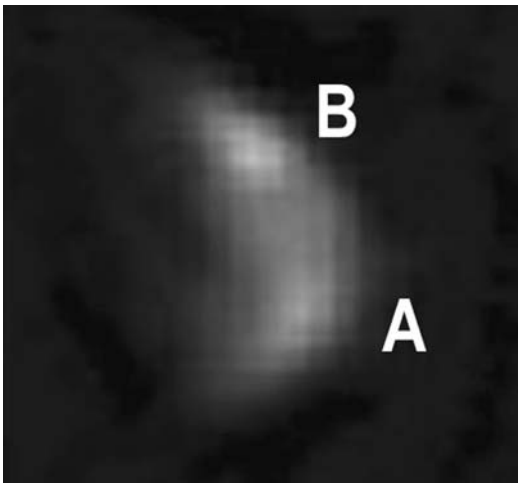

Fig. 14 Mercury image obtained by Frank Melillo, Holtzville, NY, using a red filter and small reflecting telescope. Both radar bright *spots B* and *A* are clearly seen as high albedo features in this image

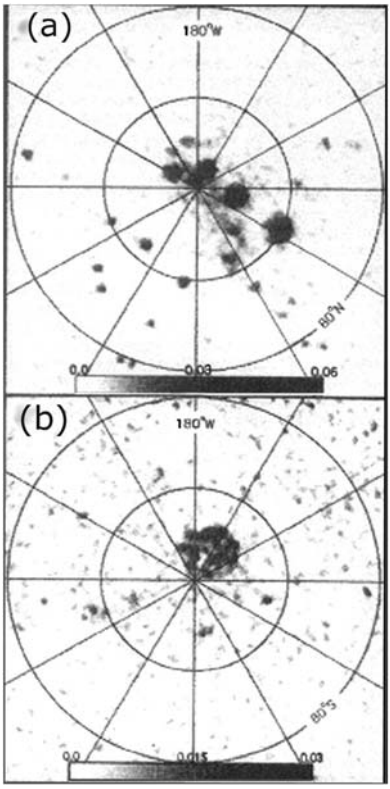

Fig. 15 High radar albedo and strong depolarization from radar backscatter indicates deposits of water ice or some other very radar-transparent material (sulfur, cold silicates, or other) in permanently shadowed craters. (**a**) north high latitudes, (**b**) south high latitudes. Figure is from Harmon et al. (1994)

interplanetary dust particles as discussed in Sect. 8. An interesting alternative is that water molecules are formed by surface chemistry interactions with the solar wind impinging on the surface and followed by a systematic, long-time migration poleward (Potter 1995).

Subsequent, very high-resolution observations (Harmon et al. 2001) showed that the highly backscattered material is found at latitudes as low as 72°N making the water ice interpretation more difficult to explain but still possible because there are regions within craters that are permanently protected from insolation by steep walls and possible rocky debris.

The necessary physical property of any material responsible for the high albedo, depolarized radar backscatter is that it has low dielectric loss at temperatures where it is observed. Another substance with the necessary dielectric property is sulfur. Sprague et al. (1995) pointed out that sulfur is not as volatile as H_2O ice and that it should be abundant in impacting and vaporizing micrometeorites and/or may be sputtered from minerals such as sphalerite in the surface regolith. Migration and cold-trapping would naturally follow. They suggest that the discovery of S in Mercury's exosphere would be a strong indicator that S is the highly backscattered material in the permanently shadowed regions. Butler (1997) argued that the latitude range of stability for S is so great that there should be S polar caps if S is the backscattering material. Cold low-iron and low-Ti silicates also have the desired low-loss character at cold temperatures (Starukhina 2001). Because silicates are ubiquitous on Mercury's surface, the coherent backscatter may not require any volatile substance. This is one of the most exciting puzzles to be answered by MESSENGER and/or Bepi Colombo.

11 Surface Evidence for a Collisional Formation Scenario and Possible Implications

Ground-based images of Mercury in the sector 70° to 150°E longitude, a region not imaged by Mariner 10, show a large, double-rimmed basin whose inner portion extends 1,000 km across with a total dimension of the outer eroded rim slightly more than 2,000 km (extending over 55° to 115°E longitude and from 40°N to 20°S). Images of this basin can be seen in Ksanfomality et al. (2007, this volume). This basin includes and extends west and north of the dark albedo feature known as Solitudo Criophori and was unofficially called "Skinakas" after the observatory from which it was first imaged by Ksanfomality (1998). The inner basin extends from 73° to 97°E and from about 30°N to 5°S. Some regions within the basin have eroded circular rims that lack rayed structure or evidence of ejecta material (Ksanfomality and Sprague 2007 and the references therein) and apparently confirmed by recent radar imaging data (cf. Fig. 38 in Harmon et al. 2007).

The impact scenario has been studied in detail in vast numerical simulations by Benz (2007, this issue) for low relative velocities and can be invoked for explanation of the following important observations and their interpretations: the loss of a substantial part of the silicate crust (Benz et al. 1988).

Based on the impact hypothesis, we can speculate that specific properties of Mercury's surface morphology and magnetic field could be related in some way to its formation. In the course of a major collision during the accretionary period, perhaps the assymetric figure and remnant fields were formed (Ksanfomality and Sprague 2007). The measured global magnetic asymmetry of the planet is known (Connerney and Ness 1988). It is possible that future observations may reveal a global non-spherical anomaly in the gravitational field correlated with the planetary magnetic field dipole offset and the location of the basin. Any surface manifestations of this collision (roughness of the surface, composition, reflectance, color, etc.) have since been probably lost, however, because of the long time exposure to subsequent secondary bombardment processes which is thought to be in excess of 3.5 billion years (Strom and Sprague 2003).

The huge basin (called Skinakas by Ksanfomality 2002, 2003), and Basin S by Ksanfomality and Sprague 2007) is located on the short axis of the assymetric figure of the planet.

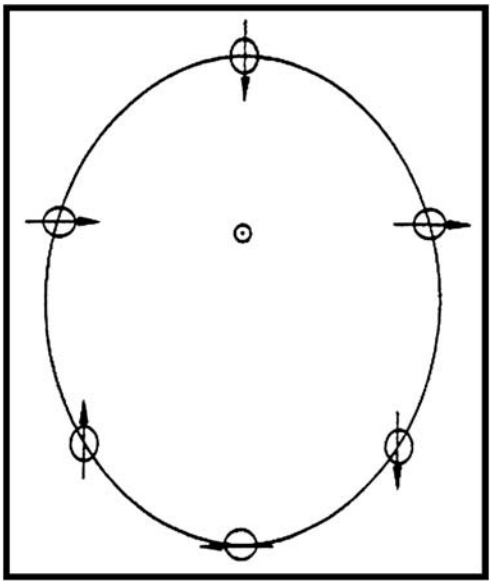

Fig. 16 The axial asymmetry of Mercury responsible for its 3 : 2 spin : orbit resonance is shown in exaggerated form above (adapted from Peale 1976). The shape is consistent with available data about the internal structure and inertia moments of the planet (van Hoolst et al. 2007, this issue)

It has apparent dark-colored regions of undetermined composition and age. The hypothesis that the present-day Mercury is a result of collisions between comparable planet-sized bodies early in the history of the Solar system may be supported by the presence of this basin once its chronology is known following the MESSENGER and Bepi Colombo missions. Partial melting, fragmentation, evaporation, re-aggregation, and gravitational escape of material on such a body is conceivable and may have been responsible for the capture of Mercury in the 3 : 2 resonance between orbital and proper rotation periods as illustrated in Fig. 16.

12 Summary Statement

The spacecraft measurements promised by the MESSENGER and Bepi Colombo missions are badly needed to augment what is known about Mercury's surface. As we have described here, Mercury's surface is likely to have regions with rocks containing Na-rich feldspar with significant Mg-rich or Ca-rich pyroxene. FeO content is likely to be of the order of at most a couple of percent by weight on most of the surface, but may be greater locally at small scales. All evidence for npFe^0 iron is circumstantial and inferred from other planetary bodies. We do not know the composition of the material in the permanently shadowed crater regions. We do not know the extent of magmatic resurfacing or the age of surface units although cratering indicates that the original bulk surface is ancient, close to 3.5 billion years old. However, a constant addition of solar wind, meteoritic and cometary material has undoubtedly considerably altered the upper most layer.

References

J. Benkhoff, J. Helbert, the MERTIS team, Adv. Space Res. **38**(4) 647–658 (2006)
M.S. Bentley, A.J. Ball, M.D. Dyar, C.M. Pieters, I.P. Wright, J.C. Zarnecki, Lunar Planet. Sci. **XXXVI** (2005)

W. Benz, Space Sci. Rev. (2007, this issue). doi:10.1007/s11214-007-9284-1
W. Benz, W.L. Slattery, A.G.W. Cameron, Icarus **74**, 516–528 (1988)
T.A. Bida, R.M. Killen, T.H. Morgan, Nature **404**, 159–161 (2000)
D.T. Blewett, P.G. Lucey, B.R. Hawke, G.G. Ling, M.S. Robinson, Icarus **129**, 217–231 (1997)
D.T. Blewett, B.R. Hawke, P.G. Lucey, Meteorit. Planet. Sci. **37**, 1245 (2002)
A.L. Broadfoot, D.E. Shemansky, S. Kumar, Geophys. Res. Lett. **3**, 577–580 (1976)
M. Bruno, G. Cremonese, S. Marchi, Planet. Space Sci. (2006, in press)
R.G. Burns, in *Remote Geochemical Analysis: Elemental and Mineralogical Composition*, ed. by C.M. Pieters, P.A.J. Englert (Cambridge University Press, Cambridge, 1993), pp. 3–29
B. Butler, D. Muhleman, M. Slade, J. Geophys. Res. **98**, 15003–15023 (1993)
B.J. Butler, J. Geophys. Res. **102**, 19,283–19,291 (1997)
M.J. Cintala, J. Geophys. Res. **97**, 947–973 (1992)
J.E. Conel, J. Geophys. Res. **74**, 1614–1634 (1969)
B. Cooper, A. Potter, R. Killen, T. Morgan, J. Geophys. Res. **106**, 32,803–32,814 (2001)
B.L. Cooper, J.W. Salisbury, R.M. Killen, A.E. Potter, J. Geophys. Res. **107**(E4), 1-1 (2002). doi:10.1029/2000JE001462
J.E.P. Connerney, N.F. Ness, in *Mercury*, ed. by F. Vilas, C. Chapman, M. Matthews (University of Arizona Press, Tucson, 1988), pp. 429–460
G. Cremonese, M. Bruno, V. Mangano, S. Marchi, A. Milillo, Icarus **177**, 122–128 (2005)
G. Cremonese et al., Space Sci. Rev. (2007, this issue). doi:10.1007/s11214-007-9231-1
D.H. Crider, R.M. Killen, Geophys. Res. Lett. **32**(L12201), xx–xx (2005). doi:10.1029/2005GL022689
N. Da Deppo, V.G. Cremonese, E. Flamini, SPIE Proc. **6265**, 626527-1/9 (2006)
N. Divine, J. Geophys. Res. **98**(E9), 17029–17048 (1993)
R.T. Dodd, *Meteorites: A Petrologic-Chemical Synthesis* (Cambridge University Press, Cambridge, 1981), p. 368
K. Donaldson-Hanna et al. (2006). http://deneb.bu.edu/mercury/
D.C. Delcourt, S. Grimald, F. Leblanc, J.-J. Berthelier, A. Milillo, A. Mura, S. Orsini, T.E. Moore, Ann. Geophys. **21**, 1723–1736 (2003)
J.P. Emery, A.L. Sprague, F.C. Witteborn, J.E. Colwell, R.W.H. Kozlowski, D.H. Wooden, Icarus **136**, 104–123 (1998)
B. Fegley Jr., A.G.W. Cameron, Earth Planet. Sci. Lett. **82**, 207–222 (1987)
S.J. Gaffey, L.A. McFadden, D. Nash, C.M. Pieters, in *Remote Geochemical Analysis: Elemental and Mineralogical Composition*, ed. by C.M. Pieters, P.A.J. Englert (Cambridge University Press, Cambridge, 1993), pp. 43–77
M.V. Gerasimov, B.A. Ivanov, O.I. Yakovlev, Earth Moon Planets **80**(1/3), 209–259 (1998)
K.A. Goettel, in *Mercury*, ed. by F. Vilas, C. Chapman, M. Matthews (University of Arizona Press, Tucson, 1988), pp. 613–621
R.E. Gold et al., Planet. Space Sci. **49**, 1467–1479 (2001)
B. Hapke, J. Geophys. Res. **101**(E7), 16,817–16,831 (1996)
B. Hapke, W. Cassidy, E. Wells, Moon **13**, 339 (1975)
B. Hapke, J. Geophys. Res. **106**, 10039 (2001)
B. Hapke, Icarus **157**, 523 (2002)
J.K. Harmon, Adv. Space Res. **19**, 1487–1496 (1997)
J.K. Harmon, M.A. Slade, Science **258**, 640–642 (1992)
J.K. Harmon, M.A. Slade, R.A. Velez, A. Crespo, M.J. Dryer, J.M. Johnson, Nature **369**, 213–215 (1994)
J.K. Harmon, P.J. Perillat, M.A. Slade, Icarus **149**, 1–15 (2001)
J.K. Harmon, M.A. Slade, B.B. Butler, J.W. Head III, D.B. Rice, M.S. Campbell, Icarus **187**, 374–405 (2007)
D.L. Harris, in *Planets and Satellites*, ed. by G.P. Kuiper, B.M. Middlehurst (The University of Chicago Press, Chicago, 1961), pp. 272
J. Helbert, L. Moroz, A. Maturilli, A. Bischoff, J. Warell, A. Sprague, E. Palomba, Adv. Space Res. (2007, in press)
B.G. Henderson, B.M. Jakosky, J. Geophys. Res. **99**(E9), 19,063–19,073 (1994)
B.G. Henderson, B.M. Jakosky, J. Geophys. Res. **102**(E3), 6567–6580 (1997)
D.M. Hunten, T.H. Morgan, D. Shemansky, in *Mercury*, ed. by F. Vilas, C. Chapman, M. Matthews (University of Arizona Press, Tucson, 1988), pp. 562–612
W.M. Irvine, T. Simon, D.H. Menzel, C. Pikoos, A.T. Young, Astron. J. **73**, 807 (1968)
R. Jeanloz, D.L. Mitchell, A.L. Sprague, I. de Pater, Science **268**, 1455–1457 (1995)
K. Kabin, T.I. Gombosi, D.L. DeZeeuw, K.G. Powell, Icarus **143**, 397–406 (2000)
E. Kallio, P. Janhunen, Geophys. Res. Lett. **30**, xx–xx (2003). doi:10.1029/2003GL017842
R.M. Killen, A.E. Potter, P. Reiff, M. Sarantos, B.V. Jackson, P. Hick, B. Giles, J. Geophys. Res. **106**, 20509–20525 (2001)

R.M. Killen, M. Sarantos, A.E. Potter, P. Reiff, Icarus **171**, 1–19 (2004)
R.M. Killen et al., Adv. Space Res. (2007). doi:10.1007/s11214-007-9232-0
P.L. Koehn, A.L. Sprague, Planet. Space Sci. (2006, in press)
G.A. Krasinsky, E.V. Pitjeva, M.V. Vasilyev, E.I. Yagudina, Icarus **158**, 98–105 (2002)
L.V. Ksanfomality, Sol. Syst. Res. **32**, 133–140 (1998)
L.V. Ksanfomality, Sol. Syst. Res. **36**, 267–277 (2002)
L.V. Ksanfomality, Sol. Syst. Res. **37**, 514–525 (2003)
L.V. Ksanfomality, A.L. Sprague, Icarus **188**, 271–287 (2007)
L.V. Ksanfomality et al., Space Sci. Rev. (2007, this issue)
H. Lammer, P. Wurz, M.R. Patel, R. Killen, C. Kolb, S. Massetti, S. Orsini, A. Milillo, Icarus **166**, 238–247 (2003)
Y. Langevin, Planet. Space Sci. **45**, 31–38 (1997)
Y. Langevin, J.R. Arnold, Annu. Rev. Earth Planet. Sci **5**, 449–489 (1977)
F. Leblanc, R.E. Johnson, Icarus **164**, 261–281 (2003)
J.S. Lewis, Earth Planet. Sci. Lett. **15**, 286–290 (1972)
J.S. Lewis, in *Mercury*, ed. by F. Vilas, C. Chapman, M. Matthews (University of Arizona Press, Tucson, 1988), pp. 651–667
L.M. Logan, G.R. Hunt, J. Geophys. Res. **75**, 6539–6548 (1970)
P.G. Lucey, D.T. Blewett, B.R. Hawke, J. Geophys. Res. **103**, 3679–3699 (1998)
P.G. Lucey, D.T. Blewett, B.L. Jolliff, J. Geophys. Res. **105**(E8), 20297–20305 (2000)
V. Mangano, A. Milillo, A. Mura, S. Orsini, E. De Angelis, A.M. Di Lellis, P. Wurz, Planet. Space Sci. (2007, in press)
I. Mann, A. Krivov, H. Kimura, Icarus **146**, 568 (2000)
I. Mann, H. Kimura, D.A. Biesecker, B.T. Tsurutani, E. Grün, R.B. McKibben, J. Liou, S. Marchi, A. Morbidelli, G. Cremonese, Astron. Astrophys. **431**, 1123 (2005)
S. Marchi, A. Morbidelli, G. Cremonese, Astron. Astrophys. **431**, 1123–1127 (2005)
S. Massetti, S. Orsini, A. Milillo, A. Mura, E. De Angelis, H. Lammer, P. Wurz, Icarus **166**(2), 229–237 (2003)
A. Maturilli, J. Helbert, A. Witzke, L. Moroz, Planet. Space Sci. **54**(11), 1057–1064 (2006a)
A. Maturilli, J. Helbert, L. Moroz, Planet. Space Sci. (2006b, in press)
T.B. McCord, J.B. Adams, Icarus **17**, 585 (1972a)
T.B. McCord, J.B. Adams, Science **178**, 745 (1972b)
T.B. McCord, R.N. Clark, J. Geophys. Res. **84**, 7664–7668 (1979)
M. Meyer, Int. Comet Q. **25**, 115 (2003)
D. Mitchell, I. de Pater, Icarus **110**, 2–32 (1994)
J.I. Moses, K. Rawlins, K. Zahnle, L. Dones, Icarus **137**, 197–221 (1999)
M. Müller, S.F. Green, N. McBride, D. Koschnyb, J.C. Zarnecki, M.S. Bentley, Planet. Space Sci. **50**, 1101–1115 (2002)
A. Mura, S. Orsini, A. Milillo, D. Delcourt, S. Massetti, E. DeAngelis, Icarus **175**, 305–319 (2005)
A.A. Mura, S. A. Milillo, S. Orsini, S. Massetti, Planet. Space Sci. (2006, in press)
J.F. Mustard, J.E. Hays, Icarus **125**(1), 145–163 (1997)
S.K. Noble, C.M. Pieters, *Mercury: Space Environment, Surface, and Interior Workshop* (Lunar and Planetary Institute, Chicago, 2001), pp. 68–69
S.K. Noble, C.M. Pieters, Sol. Syst. Res. **37**, 31 (2003)
D.A. Paige, S.E. Wood, A.R. Vasavada, Science **258**, 643–646 (1992)
S.J. Peale, Icarus **28**, 459–467 (1976)
C.M. Pieters, P.A.J. Englert, *Remote Geochemical Analysis, Elemental and Mineralogical Composition* (Cambridge University Press, Cambridge, 1993)
A.E. Potter, Geophys. Res. Lett. **22**, 3289–3292 (1995)
A.E. Potter, T.H. Morgan, Science **248**, 835–838 (1990)
B. Rava, B. Hapke, Icarus **71**, 387–429 (1987)
M.S. Robinson, P.G. Lucey, Science **275**, 197–200 (1997)
M.S. Robinson, G.J. Taylor, Meteorit. Planet. Sci. **36**, 841–847 (2001)
J.W. Salisbury, B. Hapke, J.W. Eastes, J. Geophys. Res. **92**(B1), 702–710 (1987)
J.W. Salisbury, L.S. Walter, D.M. D'Aria, *Infrared (2.1–25 μm) Spectra of Minerals* (Johns Hopkins Univ. Press, Baltimore, 1991), 267 pp
J.W. Salisbury, A. Wald, D.M. D'Aria, J. Geophys. Res. **99**, 11897–11911 (1994)
A.G. Santo et al., Planet. Space Sci. **49**, 1481–1500 (2001)
Z. Sekanina, Astrophys. J. **545**, L69 (2000)
Z. Sekanina, Astrophys. J. **597**, 1237 (2003)
E.M. Sieveka, R.E. Johnson, Astrophys. J. **287**, 418–426 (1984)

P. Sigmund, Phys. Rev. **184**, 383–416 (1969)
M. Slade, B. Butler, D. Muhleman, Science **258**, 635–640 (1992)
M. Sarantos, P.H. Reiff, T.W. Hill, R.M. Killen, A.L. Urquhart, Planet. Space Sci. **49**, 1629–1635 (2001)
G. Siscoe, L. Christopher, Geophys. Res. Lett. **2**, 158–160 (1975)
J.A. Slavin, R.E. Holzer, J. Geophys. Res. **84**, 2076–2082 (1979)
S.C. Solomon, Phys. Earth Planet. Int. **15**, 135–145 (1977)
S.C. Solomon et al., Planet. Space Sci. **49**, 1445–1465 (2001)
A.L. Sprague, J. Geophys. Res. **97**, 18,257–18,264 (1992a)
A.L. Sprague, J. Geophys. Res. **98**, E1 1231 (1992b)
A.L. Sprague, T.L. Roush, Icarus **133**, 174–183 (1998)
A.L. Sprague, S.S. Massey, Planet. Space Sci. (2006, in press)
A.L. Sprague, R.W.H. Kozlowski, D.M. Hunten, Science **249**, 1140–1143 (1990)
A.L. Sprague, R.W.H. Kozlowski, F.C. Witteborn, D.P. Cruikshank, D.H. Wooden, Icarus **109**, 156–167 (1994)
A.L. Sprague, D.M. Hunten, K. Lodders, Icarus **118**, 211–215 (1995)
A.L. Sprague, W.J. Schmitt, R.E. Hill, Icarus **135**, 60–68 (1998)
A.L. Sprague, J.P. Emery, K.L. Donaldson, R.W. Russell, D.K. Lynch, A.L. Mazuk, Meteorit. Planet. Sci. **37**, 1255–1268 (2002)
A.L. Sprague, R.W.H. Kozlowski, F.C. Witteborn, D.P. Cruikshank, D.H. Wooden, Icarus **109**, 156–167 (1994)
P. Spudis, J. Guest, in *Mercury*, ed. by F. Vilas, C. Chapman, M. Matthews (University of Arizona Press, Tucson, 1988), pp. 118–164
L.V. Starukhina, J. Geophys. Res. **106**(E7), 14701–14710 (2001)
R.G. Strom, A.L. Sprague, *Exploring Mercury the Iron Planet* (Springer-Praxis, Chichester, 2003), 216 pp.
L. Tepper, B. Hapke, Bull. Am. Astron. Soc. **9**, 532 (1977)
A.L. Tyler, R.W.H. Kozlowski, L.A. Lebofsky, Geophys. Res. Lett. **15**, 808–811 (1988)
T. van Hoolst, F. Sohl, I. Holin, O. Verhoeven, V. Dehant, T. Spohn, Space Sci. Rev. (2007, this issue). doi:10.1007/s11214-007-9202-6
A.R. Vasavada, D.A. Paige, S.E. Wood, Icarus **141**, 179–193 (1999)
F. Vilas, Icarus **64**, 133–138 (1985)
F. Vilas, in *Mercury*, ed. by F. Vilas, C. Chapman, M. Matthews (University of Arizona Press, Tucson, 1988), pp. 59–76
F. Vilas, T.B. T.B. McCord, Icarus **28**, 593–599 (1976)
F. Vilas, M.A. Leake, W.W. Mendell, Icarus **59**, 60–68 (1984)
C. Wagner, in *Thermal Emission spectroscopy and Analysis of Dust, Disks, and Regoliths*, ed. by M.L. Sitko, A.L. Sprague, D.K. Lynch (Astronomical Society of the Pacific, San Francisco, 2000), pp. 386
J. Warell, Icarus **156**, 303–317 (2002)
J. Warell, Icarus **161**, 199–222 (2003)
J. Warell, D.T. Blewett, Icarus **168**, 257–276 (2004)
J. Warell, A.L. Sprague, J. Emery, R.W. Kozlowski, A. Long, Icarus **180**, 201–291 (2006)
S.J. Weidenschilling, Icarus **35**, 99–111 (1978)
G.W. Wetherill, in *Mercury*, ed. by F. Vilas, C. Chapman, M. Matthews (University of Arizona Press, Tucson, 1988), pp. 670–691
P. Wurz, H. Lammer, Icarus **164**, 1–13 (2003)
P. Wurz, P. Bochsler, J.A. Paquette, F.M. Ipavich, Astrophys. J. **583**, 489–495 (2003)
P. Wurz, in *The Dynamic Sun: Challenges for Theory and Observations*, ESA SP-600, 5.2, (2005), 1–9
P. Wurz, U. Rohner, J.A. Whitby, C. Kolb, H. Lammer, P. Dobnikar, Planet. Space Sci. (2006, submitted)